Received: Added at production | Revised: Added at production | Accepted: Added at production

DOI: xxx/xxxx

FULL PAPER

Investigation of the 2D assumption in the image-based inertial impact (IBII) test

Jared Van Blitterswyk* | Lloyd Fletcher | Fabrice Pierron

[1]Mechanical Engineering, University of Southampton, Southampton SO17 1BJ, UK

Correspondence

*Jared Van Blitterswyk, University of Southampton, University Road, Southampton SO17 1BJ, UK, Email: j.van-blitterswyk@soton.ac.uk

Abstract

The image-based inertial impact (IBII) test has shown promise for measuring properties of composites at strain rates where existing test methods become unreliable due to inertial effects ($>10^2$ s^{-1}). Typically the IBII tests are performed with a single camera and therefore, to use surface measurements for material property identification it is necessary to assume that the test is two-dimensional. In this work, synchronised ultra-high speed cameras are used to quantify the relevance of this assumption when non-uniform, through-the-thickness loading is applied to interlaminar samples. Initial experiments revealed that an angular misalignment of approximately 1° between the impact faces of the waveguide and projectile created a bending wave that propagated along the sample behind the axial pulse. Even under these conditions, consistent measurements of stiffness were made by assuming a linear distribution of the behaviour through-the-thickness. When the misalignment was reduced to 0.2° the effects on single-sided measurements were significantly reduced. The two alignment cases were compared to show that three-dimensional loading had a small effect on stiffness identification (approx. 5% bias) relative to failure stress (approx. 30% bias). This study highlights the importance of impact alignment for reliable characterisation of the interlaminar failure stress, and was used to establish guidelines for diagnosing loading issues from single-sided measurements.

KEYWORDS:

image-based inertial impact (IBII) test; fibre-reinforced polymer composites; high strain rate; interlaminar properties; ultra-high-speed imaging

1 | INTRODUCTION

The widespread use of polymer-matrix composites for primary load-bearing structures often requires design consideration for dynamic loading (*e.g.:* blast, crash, foreign object strike, *etc.*). Under these conditions significant interlaminar stresses can be generated over a wide range of strain rates. In many blast and crash applications the strain rates of interest range from a few 10's to several thousands of inverse seconds. To develop useful simulations for single and multi-material composite structures under these loading conditions, the sensitivity of interlaminar constitutive properties to strain rate must be established experimentally. Literature suggests that that stiffness and strength of polymer matrix materials exhibit a moderate sensitivity to strain rate [1, 2]; however, the number of studies attempting to measure high-strain-rate interlaminar properties are scarce and inconsistent [2].

Part of this is a result of limited test development specifically for interlaminar characterisation. The common approach has been to adopt in-plane test configurations, however, these tests are difficult to scale down and suffer from issues with gripping, misalignment and high sensitivity to specimen machining defects [3]. High-strain-rate testing with traditional test methods (*i.e.*: Kolsky bar and high-speed load frames) have additional issues with managing specimen inertia generated by dynamic loading. For example, with the Kolsky bar test, it is necessary to assume a state of quasi-static stress equilibrium. This condition is not satisfied until the inertia in the sample dampens out. This occurs after several reverberations of the pulse within the sample, and the time required for this to occur is dependent on the wave speed [4, 5]. For low wave speed materials, such as polymer matrix composites in the interlaminar planes, it is generally accepted that Kolsky bar apparatus is not able to provide a true measurement of the initial stiffness [5–8]. The inertial effects may also persist throughout the entire duration of the test, which may render strength measurements unreliable in composites where failure strains are small. Inertia is thought to be the largest contributor to the high amounts of scatter in reported measurements of stiffness and strength in the literature as documented in the review by Van Blitterswyk *et al.* [2].

A number of recent experimental studies have combined ultra-high-speed imaging with full-field measurement techniques for high-strain-rate material characterisation [10–20]. In these studies, full-field maps of acceleration were processed using the virtual fields method (VFM) to directly identify the properties of the material. In doing so, the specimen acted as a load cell, and stress was reconstructed without needing to measure force externally. Full-field measurements remove the requirement of quasi-static stress equilibrium, and thus allow for a significant increase in strain rates at which materials can be tested. The idea of using full-field measurements and the VFM for high strain rate testing was initially explored by Moulart *et al.* [9] and Pierron & Forquin [10]. Since then, the concept has been developed into the image-based inertial impact (IBII) test, which has been used for characterising the in-plane properties of composites [11, 13, 14], the interlaminar properties of composites [15], and ceramics [16].

As part of continued development of the IBII test methodology, it is important to understand how well the underlying assumptions are satisfied, and identify scenarios where they may break down. In order to use surface measurements to directly identify material properties in the IBII test, the key assumptions are: 1) kinematic fields are uniform through the thickness dimension of the sample; and 2) the specimen can be considered to be in a state of plane stress. These assumptions are difficult to validate with surface measurements as they may have embedded three-dimensional effects. The primary objective of this study is to use ultra-high-speed imaging to simultaneously measure the response on the front and back faces to verify the assumption of through-thickness uniformity for the interlaminar test configuration presented in [15]. The interlaminar specimens provide a challenging test case for this assumption as the samples are generally less slender compared to the in-plane tests in [14], and stage position tolerance becomes larger relative to the components in the impact chain. From a practical perspective, most experiments will be performed with a single camera. Therefore, an additional objective of this work is to establish diagnostics for single-sided measurements to identify when measurement assumptions are not well satisfied.

2 | TEST PRINCIPLE AND THEORY

In an IBII test the specimen is loaded with a dynamic pulse generated from a projectile impact. The general arrangement for an interlaminar IBII test is shown in Fig. 1. The impact creates a compressive pulse in the sample that travels towards the free edge. At the free edge, it reflects as a tensile pulse, which unloads the material. For materials with greater strength in compression than in tension, this can be exploited to create a spall fracture in the sample using the reflected pulse. A regular grid pattern is deposited on the surface of each sample and images of the grids are collected during the test using an ultra-high-speed camera. The images are processed using the grid method to calculate full-field maps of displacement, from which strains and accelerations are derived. Using the VFM it is possible to identify stiffness and failure stress directly from the measured fields, as described in the following sections.

2.1 | The Virtual Fields Method

The VFM is a well-documented inverse method for extracting material properties from full-field measurements [21]. Previous studies by the authors [14, 15] outline the specific application of the VFM for the IBII test, and therefore, only key concepts will be provided here for completeness. For brevity, time and space dependence is omitted unless necessary in the following derivations. The general form of the principle of virtual work, neglecting body forces, is given by:

$$-\int_V \boldsymbol{\sigma} : \boldsymbol{\epsilon}^* dV + \int_{\delta S} \boldsymbol{T} \cdot \boldsymbol{u}^* dS = \int_V \rho \boldsymbol{a} \cdot \boldsymbol{u}^* dV \tag{1}$$

where V denotes the volume of the region of interest, $\boldsymbol{T}$ is the Cauchy stress vector, which is applied to the in-plane boundaries denoted by δS, ρ is the material density, $\boldsymbol{a}$ the acceleration field, $\boldsymbol{\sigma}$ is the Cauchy stress tensor, $\boldsymbol{u}^*$ is the virtual displacement field, and $\boldsymbol{\epsilon}^*$ the virtual strain field deriving from the virtual displacement fields through $\epsilon^*_{ij} = 1/2(u^*_{i,j} + u^*_{j,i})$. The VFM relies on selecting specific virtual fields to generate integral equilibrium equations, with the underpinning idea that with full-field kinematic measurements, integrals can be approximated by discrete sums. More details can be found in [21].

2.2 | Two-dimensional stress approximation (membrane stress)

Stiffness and failure stress identifications from an IBII test are performed under the following assumptions: 1) constant density and thickness in space; and 2) plane stress loading. When only single-sided measurements are available, as in previous work [14–16], it is also necessary to assume that the test is two-dimensional (*i.e.*: surface measurements are representative of the through-thickness behaviour); however, with back-to-back measurements this assumption is not necessary. Under two-dimensional conditions Eq. (1) takes on the form in Eq. (2):

$$-\int_S \boldsymbol{\sigma} : \boldsymbol{\epsilon}^* dS + \int_{\delta l} \boldsymbol{T} \cdot \boldsymbol{u}^* dl = \rho \int_S \boldsymbol{a} \cdot \boldsymbol{u}^* dS \tag{2}$$

where δl denotes the line boundary over which the Cauchy stress vector is applied. Using the simplest case of a rigid-body virtual field: $u^*_x = 1$, $u^*_y = u^*_z = 0$, the contribution of internal virtual work is removed (zero virtual strains) and $\boldsymbol{T} \cdot \boldsymbol{u}^*$ in Eq. (2) is written as:

$$\boldsymbol{T} \cdot \boldsymbol{u}^* = \begin{pmatrix} \sigma_{xx} \\ 0 \\ 0 \end{pmatrix} \tag{3}$$

Recall from Fig. 1 that $x = 0$ corresponds to the vertical free edge of the sample ($\sigma_{xx} = 0$). Substituting Eq. (3) into Eq. (2) provides a direct relationship between the axial stress along a vertical slice in the sample at position x_o:

$$\int_{-H/2}^{H/2} \sigma_{xx}(x = x_0) dy = \rho \int_{-H/2}^{H/2} \int_{0}^{x_0} a_x u^*_x dx dy \tag{4}$$

If full-field displacements are measured with sufficient spatial resolution, the integral quantities can be estimated using discrete sums. For example, the right hand side of Eq. (4) is approximated as,

$$\rho \int_{-H/2}^{H/2} \int_{0}^{x_0} a_x dx dy \approx \rho x_o H \overline{a_x}^S \tag{5}$$

where the superscript S coupled with an overline denotes the surface average between the free edge and x_o. The line integral on the left hand side of Eq. (4) represents the average stress along the cross-section (denoted by overline with a superscript y), and Eq. (4) becomes:

$$\overline{\sigma_{xx}}^y(t) = \rho x_o \overline{a_x(t)}^S \tag{6}$$

which is commonly referred to as the 'stress-gauge' equation [11, 16]. Plotting the average axial stress from Eq. (6) as a function of the average axial strain in the cross-section at position x_0, neglecting stress along the fibre direction as in [14] one can interrogate the stress-strain response at any cross section along the length of the sample. Using a linear regression fit to the compression loading response provides a spatial identification of the interlaminar elastic modulus E_{33}. Spatial smoothing effects influence the measurements within one kernel at the impact and free edges. Low stress near the free edge and Saint-Venant effects present near the impact edge compound with smoothing to reduce the stability of the identification in these regions. To avoid including these effects, the stiffness value for the test is generally taken as the average identification from cross-sections between $x = 0.25L$ and $0.75L$. It should be noted that Eq. (6) can also be used for failure stress estimation if σ_{xx} does not depend on y.

In the case that σ_{xx} depends on y, a linear approximation of the stress distribution across the width of the sample can be reconstructed by considering the virtual field used to derive Eq. (6), and additional rigid-body virtual fields ($u_x^* = 0$, $u_y^* = 1$, and $u_x^* = y$, $u_y^* = -x$) as fully documented in [14]. This is referred to as the 'linear stress-gauge' (LSG) equation (Eq. (7)):

$$\sigma_{xx}(LSG) = \rho x_o \overline{a_x}^S + \frac{12 \rho x_o y}{H^2} (\overline{a_x y}^S - \overline{a_y x}^S + x_o \overline{a_y}^S) \tag{7}$$

where H denotes the total specimen width (Fig. 1). The common approach used to estimate failure stress is to take the maximum stress from Eq. (7) within a small virtual gauge window (20 × 30 pixels) centred on the crack initiation location [14, 15].

Stress can also be reconstructed from strain maps using the identified stiffness parameters and the assumed linear-elastic constitutive model. It was shown in [14] that for highly anisotropic carbon-epoxy unidirectional composites tested with the IBII test at 90°, the effect of stresses in the fibre direction can be neglected and so::

$$\sigma_{xx}(\epsilon_{xx}) = E_{33} \epsilon_{xx} \tag{8}$$

The strain-based stress reconstruction is useful for identifying cases when the constitutive model or measurement assumptions break down. For example, damage/fracture can be detected by a divergence of the strain-based and acceleration-based stress reconstructions. As will be shown, it can also be used to assess whether the test is two-dimensional since through-thickness heterogeneity also causes a divergence of the stress reconstructions.

2.3 | Through-thickness effects (bending & membrane stress)

Eq. (6)-(7) are valid only if the stresses and strains are uniform through-the-thickness. If this is not the case, it is possible to combine the VFM with thin-plate theory to reconstruct a linear approximation of stress through-the-thickness under the assumption of plane stress loading. Here we denote the z axis origin along the mid-plane of the sample. The displacement (u_x, u_y), acceleration (a_x, a_y), strain (ϵ_{xx}, ϵ_{yy}, ϵ_{xy}) and stress fields (σ_{xx}, σ_{yy}, σ_{xy}) are written as a function of their membrane (mid-plane) $\boldsymbol{x}^o$ and flexural $\boldsymbol{x}^f$ components in the following general form:

$$\boldsymbol{x}(x, y, z, t) = \boldsymbol{x}^o(x, y, t) + \frac{2z}{e}\boldsymbol{x}^f(x, y, t) \tag{9}$$

where e denotes the specimen thickness (see Fig. 1). The out-of-plane component for u_z, and a_z are written as:

$$\begin{cases} u_z(x, y, t) = u_z^o(x, y, t) \\ a_z(x, y, t) = a_z^o(x, y, t) \end{cases} \tag{10}$$

To simplify notations, the functions will now be written without their variables but follow what has just been defined. The membrane and flexural components of displacement (u_x, u_y) can be derived from front and back face measurements according to:

$$\begin{cases} \boldsymbol{u}^o = \frac{1}{2}(\boldsymbol{u}^F + \boldsymbol{u}^B) \\ \boldsymbol{u}^f = \boldsymbol{u}^F - \boldsymbol{u}^o \end{cases} \tag{11}$$

where superscripts 'F' and 'B' denote the front face (z = +$e/2$) and back face (z = -$e/2$). These quantities are spatially differentiated to obtain in-plane strain components ($\boldsymbol{\epsilon}$: $\epsilon_{xx}, \epsilon_{yy}, \epsilon_{xy}$):

$$\boldsymbol{\epsilon} = \boldsymbol{\epsilon}^o + \frac{2z}{e}\boldsymbol{\epsilon}^f \tag{12}$$

where ϵ^o and ϵ^f denote the membrane and flexural strain components, respectively. The displacements are also twice differentiated temporally to obtain in-plane acceleration components ($\boldsymbol{a}$: a_x, a_y):

$$\boldsymbol{a} = \boldsymbol{a}^o + \frac{2z}{e}\boldsymbol{a}^f \tag{13}$$

As a first step, this formulation for the field quantities will be used to recover Eq. (6) from the full 3D version of the principle of virtual work. Substituting the same rigid-body virtual field ($u_x^* = 1$, $u_y^* = u_z^* = 0$) in Eq. (1) results in:

$$\int_{-e/2}^{e/2}\int_{-H/2}^{H/2} \sigma_{xx} dydz = \rho \int_{-e/2}^{e/2}\int_{-H/2}^{H/2}\int_{0}^{x_0} a_x dxdydz \tag{14}$$

Replacing a_x and σ_{xx} by the linear combination of the membrane and flexural components results in:

$$\int_{-e/2}^{e/2}\int_{-H/2}^{H/2} \left(\sigma_{xx}^o + \frac{2z}{e}\sigma_{xx}^f\right) dydz = \rho \int_{-e/2}^{e/2}\int_{-H/2}^{H/2}\int_{0}^{x_0} \left(a_x^o + \frac{2z}{e}a_x^f\right) dxdydz \tag{15}$$

Since the integration of the linear terms in z comes to zero, this expression simplifies to Eq. (16), which represents an equivalent form of the stress-gauge equation for width-averaged membrane stress as a function of membrane acceleration:

$$\overline{\sigma_{xx}^o}^y = \rho x_0 \overline{a_x^o}^S \tag{16}$$

Therefore, if a_x^F and a_x^B are measured, then $a_x^o = 1/2(a_x^F + a_x^B)$ and $\overline{\sigma_{xx}^o}^y$ can be calculated without bias. Moreover, this can then be plotted against the membrane component of strain ($\epsilon_{xx}^o = 1/2(\epsilon_{xx}^F + \epsilon_{xx}^B)$) to obtain the stress-strain response, from which stiffness can be identified without bias. However, even if σ_{xx} does not depend on y, it may depend on z and therefore, $\overline{\sigma_{xx}^o}^y$ will not be a good approximation for failure stress. Therefore, the question becomes: "can we identify σ_{xx}^f from back-to-back acceleration measurements?" To do this, we introduce a rigid-body rotation virtual field about the y axis ($u_x^* = z$, $u_y^* = u_z^* = -x$). In this case:

$$\boldsymbol{T} \cdot \boldsymbol{u}^* = \begin{pmatrix} \sigma_{xx} z \\ 0 \\ -\sigma_{xz} x \end{pmatrix} \tag{17}$$

Substituting Eq. (17) into Eq. (1), assuming σ_{xz} can be neglected (Love-Kirchhoff thin plate theory) results in:

$$\int_{-e/2}^{e/2}\int_{-H/2}^{H/2}\left(\sigma^{o}_{xx}z+\frac{2z^2}{e}\sigma^{f}_{xx}\right)dydz=\rho\int_{-e/2}^{e/2}\int_{-H/2}^{H/2}\int_{0}^{x_0}\left(a^{o}_{x}z+\frac{2z^2}{e}a^{f}_{x}-a^{o}_{z}x\right)dxdydz \tag{18}$$

Again, the linear term in z integrates to zero and the equation simplifies to give the width-averaged flexural stress component as a function of acceleration (Eq. (19)).

$$\overline{\sigma^{f}_{xx}}^{y}=\rho x_0\left(\overline{a^{f}_{x}}^{S}-\frac{6}{e}\overline{a^{o}_{z}x}^{S}\right) \tag{19}$$

Similarly, the linear stress-gauge equation (Eq. (7)) can be re-written for each face in terms of flexural and bending components of acceleration as in:

$$\sigma^{F,3D}_{xx}(LSG)=\rho x_o\left(\overline{a^{o}_{x}}^{S}+\overline{a^{f}_{x}}^{S}-\frac{6}{e}\overline{a^{o}_{z}x}^{S}\right)+\frac{12\rho x_o y}{H^2}\left(\overline{a^{o}_{x}y}^{S}-\overline{a^{o}_{y}x}^{S}+x_o\overline{a^{o}_{y}}^{S}\right) \tag{20}$$

$$\sigma^{B,3D}_{xx}(LSG)=\rho x_o\left(\overline{a^{o}_{x}}^{S}-\overline{a^{f}_{x}}^{S}+\frac{6}{e}\overline{a^{o}_{z}x}^{S}\right)+\frac{12\rho x_o y}{H^2}\left(\overline{a^{o}_{x}y}^{S}-\overline{a^{o}_{y}x}^{S}+x_o\overline{a^{o}_{y}}^{S}\right) \tag{21}$$

Averaging the linear stress-gauge reconstructions from both faces provides the membrane component of acceleration as:

$$\sigma^{A}_{xx}(LSG)=\rho x_o\overline{a^{o}_{x}}^{S}+\frac{12\rho x_o y}{H^2}\left(\overline{a^{o}_{x}y}^{S}-\overline{a^{o}_{y}x}^{S}+x_o\overline{a^{o}_{y}}^{S}\right) \tag{22}$$

Clearly, Eq. (19)-(21) are dependent on out-of-plane acceleration, a^{o}_{z}, which cannot be resolved from in-plane measurements. Therefore, in the presence of dynamic bending deformation, the true stress will be biased by stress reconstructed from surface measurements of acceleration. In this work, full-field measurements made with synchronised ultra-high-speed cameras will be used to quantify the bias caused by out-of-plane loading on the reconstruction of stress-strain curves, and the identification of stiffness and failure stress for the IBII test.

3 | MATERIALS AND EXPERIMENTAL SETUP

The material used in this study was the same unidirectional carbon/epoxy composite (AS4-145/MTM45-1) as was used in [15]. This laminate had a measured density of 1,605 ± 20 kg·m^{-3}. Seven samples were cut from the 1-3 interlaminar plane with dimensions (length × height × thickness) of 18.3 mm × 11.58 mm × 2.56 mm (standard deviations: ±0.03 mm, ±0.17 mm, ±0.4 mm). Specimens were painted white and black grids, with an average pitch of 0.337 mm, printed onto both sides of the sample according to [23–25]. Specimens were mounted onto the waveguides with cyanoacrylate glue using a set square for alignment during bonding. The waveguide, projectile and sabot were the same as in the previous study [15].

3.1 | Impact rig and waveguide alignment

All impact experiments were performed using the compressed air impact rig described in [14, 25]. Since the previous study, a new 5-axis platform was commissioned that enables more control over the waveguide alignment. The stand consists of several mechanical stages (Fig. 2) to adjust the yaw, pitch and 3D translations of the platform on which the foam stand and waveguide sit.

A machined alignment rod was first used to set the approximate position of the stand. The diameter of one end of the rod was machined to fit in the bore of the barrel, and the other end was machined to the same diameter as the waveguide. The stand was adjusted such that the impact face of the waveguide was flush (within visual inspection and touch) to the end of the alignment rod once inserted in the barrel. To correct for the movement of the projectile in free flight, test shots were then performed with the Shimadzu HPV-X camera to visualise the impact between the projectile and the waveguide from the side-on perspective (x-y plane as defined in Fig. 1). Images just prior to impact were processed to extract the coordinates of the top and bottom of the waveguide and projectile faces. From these coordinates, it was possible to quantify the vertical and angular misalignment of the impact faces. The stage was adjusted accordingly, and test shots repeated, until the translation and angular misalignments were below 1-pixel (uncertainty of coordinate selection), which corresponds to 0.1 mm and 0.2° for position and pitch angle, respectively.

3.2 | Synchronised ultra-high-speed imaging

Two Shimadzu ultra-high speed cameras were used to image the front face (HPV-X model) and back face (HPV-X2 model) of the sample through transparent windows in the side walls of the capture chamber. A schematic of the camera arrangement is shown in Fig. 3. Both cameras used a Sigma 105mm lens and illumination was provided by a pair of Bowens Gemini 1000pro flashes. To synchronise the flash lights and cameras, the trigger from the light gates (mounted at the end of the gas gun barrel [25]) was split and sent to each flash, and the copper contact trigger on the waveguide was sent directly to the Shimadzu HPV-X camera. The cameras were run in a master-slave configuration to synchronise the internal clocks, with the HPV-X camera used to trigger the HPV-X2. The stand-off distance of each camera was adjusted iteratively using a series of static images so that the grids were sampled by exactly 7 pixels/pitch (pitch size = 0.337 mm). This resulted in a stand-off distance of approximately 310 mm. For consistent depth-of-field, both camera apertures were set to f/11 with illumination adjusted accordingly for each camera. Less light was required for the Shimadzu HPV-X2 camera, which had a higher sensor sensitivity. To minimise fill factor effects, the images were intentionally blurred as in [14–16]. The amount of blurring was checked using a 2 mm out-of-plane movement test to ensure that no parasitic fringe patterns from the fill-factor effect were visible in the static strain images.

This back-to-back camera and flash arrangement (Fig. 3) has the drawback that the flash from one side of the capture chamber is pointed towards the camera on the other side, leading to saturation. To control the lighting on each side, a disposable light shield was installed around the sample, as shown in Fig. 4. A slot just larger than the specimen size was cut from the edge of a thin piece of board. The screen was then slotted over the specimen and fixed to the bottom of the capture chamber.

3.3 | Image processing

Images from both cameras were processed using the same procedure as described in the flow chart in Fig. 5 of [15]. Spatial and temporal smoothing parameters for each camera were selected using an image deformation sweep, as performed in [15]. The reader is also referred to [26, 27] for additional details on the image deformation procedure. In this process, synthetic images were generated that were representative of those collected with each camera (see Table A.1) in the appendix for a summary of parameters used to generate the images). These images were deformed using displacement fields from a finite element model [15] and processed with a range of spatial and temporal kernel sizes to assess the effect of smoothing on the identification of stiffness. Optimal parameters were selected as those which minimised the total error between the identified stiffness from the synthetic images and the reference value in the finite element model. The Shimadzu HPV-X2 sensor had approximately twice as much grey-level noise as the HPV-X and therefore, optimal parameters were different for each camera. Selected smoothing parameters for processing experimental images, along with typical measurement performance for each camera are listed in Table A.2.

3.4 | Coordinate transformation to common reference coordinates

A coordinate system transformation, outlined in the flow chart shown in Fig. 5, was developed to enable fields measured on the front and back faces to be directly compared. The approach was to transform the fields measured in the back face coordinate system (X^B,Y^B) to the front face coordinate system (X^F,Y^F). In each field of view the coordinates of the top corner on the free edge (x^F_{FE}, y^F_{FE} and x^B_{FE}, y^B_{FE}) was used as a common reference point. The difference between these coordinates defined the translation required (Δx^B, Δy^B) from the original back face coordinates to the equivalent position in the front face coordinates

($X^{B'}$,$Y^{B'}$). The displacement fields in the transformed coordinates were then interpolated to the same measurement locations on the front face over the common field of view. Acceleration and strain fields were then computed in the same way for both sides of the sample using the parameters defined in Table A.2. Note that no rotational transformation was performed as variations in grid orientation between the front and back of the sample were small (<1°).

4 | RESULTS

4.1 | Full-Field Measurements

Comparing full-field maps of strain and acceleration provides a quick way to assess the uniformity of loading through-the-thickness. Tests on different samples showed varying levels of differences in the kinematic fields. Specimen #1 is presented here as a case where the response was substantially different on each face to provide a clearer understanding of the evolution of through-thickness heterogeneity. In the case of the 1-3 interlaminar plane, only the x-fields are strongly activated due to high lateral stiffness of the fibres [15]. Therefore, only the axial strain and acceleration maps are presented here. Full-field maps of a_x and ϵ_{xx} are shown at three time steps for both cameras in Fig. 6 and 7, respectively. The differences between the two sides are also included for each time step. Note that the fields have been transformed to the same coordinate system using the procedure described in Section 3.4. Maps of all displacement, strain and acceleration components for each specimen are included as supplementary material with this article.

The fields at 8 μs represent the time just before the front of input pulse reached the free edge. Up until this point, only regions near the impact edge showed measurable differences (up to 2 mm·m^{-1} in width-averaged strain). As the test progressed (t = 13 μs) differences between the front and back response increased up to 10 mm·m^{-1} near the impact edge. At this point, subtle differences in the fields were also measured further into the sample (up to $x = 5$ mm). The through-thickness effects continue to propagate into the sample, and at 17 μs a clear oscillating pattern was revealed in the difference maps for acceleration and strain (Fig.6-7).

For specimen #1 it is clear that the assumption of through-thickness uniformity is not well satisfied near the impact edge but may hold near the free edge. The effect of this varying non-uniformity along the length of the sample on the reconstruction of stress-strain curves, and identifications of stiffness and failure stress is investigated in the following sections for all tested samples.

4.2 | Stress-strain curves and stiffness identification

Stress-strain curves were reconstructed along the length of each sample by combining the stress-gauge equation (Eq. (6)) with the average axial strain ($\overline{\epsilon_{xx}}^{y}$), neglecting the presence of fibre stress. This was performed separately for each face, and using back-to-back averaged fields as a linear approximation to the through-the-thickness distribution (Eq. (16) combined with $\overline{\epsilon^{o}_{xx}}^{y} = 1/2(\overline{\epsilon^{F}_{xx}}^{y} + \overline{\epsilon^{B}_{xx}}^{y})$). Note that the purpose of processing each face separately is to evaluate the consequences of having to assume stress and strain is uniform through the thickness. The through-thickness strain distribution can be closely resolved with two-sided measurements (thickness is small so strain variation will be nearly linear), however, the stress component is dependent on a_z (see Eq. (18)). Since, in all cases, we do not have the ability to identify the a_z component of acceleration, we can only infer its contribution. This is based on differences in stress reconstructions from acceleration and from strain on each face, and through comparison to tests where out-of-plane effects are reduced, as described in later sections.

Stress-strain curves from three specimens are presented at four locations in Fig. 8. These three samples were chosen to demonstrate the variability measured across the seven tests. Specimen #3 represents a case where comparatively minimal differences were observed between the front and back face measurements (Fig. 8a-8d). The remaining samples showed more significant differences between the front and back faces similar to specimen #1 (Fig. 8e-8h) and specimen #5 (Fig. 8i-8l). Note that stress plotted in Fig. 8 for single-sided measurements denotes the approximation of $\overline{\sigma_{xx}}^{y}$ assuming it can be fully expressed from measured acceleration. Alternatively, the back-to-back average denotes the membrane stress, which can be fully resolved. If no out-of-plane effects were present, the two should agree exactly.

Generally, the stress-strain curves reconstructed on each face show a reasonable agreement during the initial compressive loading, but a dramatically different unloading response. As indicated by the full-field maps (Fig. 6-7), the largest differences in loading and unloading response were measured over half of the sample closest to the impact edge ($x/L > 0.50$), though specimens #1 and #5 show appreciable differences later in the unloading response up to $x/L = 0.33$. The variability in non-uniform through-thickness loading along the length, and in the load-unload response, will influence stiffness and failure stress identifications differently. The rest of this section focuses on stiffness identification, and the failure stress identification will be discussed in the following section.

Figure 9 shows the spatial variation in the interlaminar stiffness for the three representative samples. Smoothing edge effects corrupt the measurements within one spatial smoothing kernel at the impact and free edges, which are omitted in Fig. 9. Identified stiffness values are reported in Table 1, obtained as the average over the middle 50% of each sample. It is worth noting that the three-dimensional effects caused a parasitic, non-linear stress-strain response towards peak compressive load and therefore, stiffness was calculated using a strain threshold of 8 mm·m^{-1}, where such effects were reduced.

The stiffness identifications from fields measured on both sides of specimen #3 closely agree (within 2%) up until $x/L = 0.5$. The identifications begin to diverge closer to the impact edge where three-dimensional effects are more significant. Specimen #1 and #5 show stronger three-dimensional effects, which create an offset between the identifications from the front and back faces at all locations. The stiffness from each face differs between 10% ($x/L = 0.33$) and 20% ($x/L = 0.67$). Conversely, identifications using back-to-back averaged fields remains stable over the entire sample with an average value of 10.5 GPa.

When the accelerations and strains are averaged through-the-thickness the stress-strain response becomes linear, as reported by others in [22, 28]. Moreover, the spatial variation and intra-test scatter were reduced on the identifications from back-to-back averaged fields (coefficient of variation (COV) = 2% over all samples). Back-to-back averaging for specimen #1 and #5, where 3D effects are greater, gives a very similar identification to specimen #3, with measured values of 10.6 GPa and 10.5 GPa, respectively. This shows that the linear through-thickness approximation from back-to-back averaging is a good representation of the actual distribution. This is because averaging through-the-thickness is the same as resolving the membrane component of stress and strain, which are unbiased by the three-dimensional loading as discussed in Sec. 2.3. For applications where three-dimensional loading is of concern, back-to-back cameras are recommended to reduce scatter and bias of stiffness measurements, and can be used to determine the limits of stiffness variability in single-sided measurements.

In the case that only single-sided measurements are available, the consequences of three-dimensional loading on stiffness measurements are not severe when averaged over several tests. While stiffness identifications can vary significantly for an individual test, the process of averaging over the middle 50% of the sample regularises the scatter significantly. In the case of specimens #1 and #5, the averaging process reduces the local variations (of up to 20%) down to 5-9% compared to the value identified with back-to-back averages. Further regularisation occurs with averaging over multiple samples. The difference between the average for all samples on each face, and the average identified from back-to-back averages, reduces to 3% over all seven samples. However, the user must be cognisant of the fact that the measurements may have a systematic error, as these tests show a systematically higher stiffness identification from the back face (11.0 GPa) than from the front face (10.5 GPa). The scatter on the single-sided measurements was less than 5% (COV) at strain rates on the order of 3,000 s^{-1}, which is still exceptional given the measurement inconsistencies reported with existing test methods at similar strain rates (see summary figures in [2]).

From these tests it can also be said that the bias from 3D effects on single-sided measurements may be reduced further by more strategic selection of the region over the sample used for averaging. The normalised root-mean-square (RMS) variation ($v_{RMS} = \text{RMS}(E_{33}(x) - \overline{E_{33}})/\overline{E_{33}}$ in Table 1) of the spatial identification, relative to the average over the middle 50% of the sample, is proposed here as an indicator of when this may be required. This is included in Table 1 for all samples. The RMS variation of the identifications from the front and back faces where three-dimensional effects were substantial ranged between 3-7%. In comparison, the majority of identifications made from back-to-back averages had a lower RMS variation in the range of 0.7-1.5%. In cases with high RMS variation (≥3%) the identifications were generally stable between $x/L = 0.25\text{-}0.5$, where three-dimensional effects were smaller. The average identification could be weighted towards this region to reduce measurement bias. As an example, for specimen #1 this procedure reduces the back-to-back difference in stiffness from 1.6 GPa, to 1.2 GPa. Therefore, in tests where three-dimensional effects are of concern, it is recommended that the spatial average of the identified stiffness be weighted towards the free edge, (*e.g.:* 25-50% from the free edge).

4.3 | Failure stress identification

To investigate the effect of the out-of-plane loading on failure stress estimates, similar stress reconstruction diagnostics to those in [15] are presented for specimen #1 and specimen #3. Two specimens with varying amounts of out-of-plane effects are shown to represent the range of behaviours measured across all samples. Stress was reconstructed with the linear stress-gauge equation ($\sigma_{xx}(LSG)$) using measurements made on each side of the sample assuming the test was two-dimensional (neglecting $6\overline{a_z^o x}^S/e$ in Eqs. (20) and (21)) as:

$$\sigma^F_{xx}(LSG) = \rho x_o \overline{a^F_x}^S + \frac{12\rho x_o y}{H^2}(\overline{a^F_x y}^S - \overline{a^F_y x}^S + x_o \overline{a^F_y}^S) \tag{23}$$

$$\sigma^B_{xx}(LSG) = \rho x_o \overline{a^B_x}^S + \frac{12\rho x_o y}{H^2}(\overline{a^B_x y}^S - \overline{a^B_y x}^S + x_o \overline{a^B_y}^S) \tag{24}$$

Stress was also reconstructed using back-to-back averages to evaluate the membrane component of stress ($\sigma^A_{xx}(LSG)$) using Eq. (22). From these fields, three estimates of tensile failure stress were obtained, as summarised for all tests in Table 1. The failure stress for all specimens reported in Table 1 represents the peak tensile stress within the virtual gauge on each side of the sample. Note that the size of the virtual gauge will also have an influence on failure stress identification, but it is beyond the scope of the current work to address this. The bias introduced in the failure stress estimate is far from intuitive due to the dependency on spatial smoothing within the gauge region and temporal smoothing of acceleration used to reconstruct stress. Work is currently underway to develop the framework for quantifying this error using image deformation.

Average values across specimens were found to be fairly consistent between the front, back and back-to-back averages with failure stress identified as 77.1 MPa (COV = 21%), 72.7 MPa (COV =25%) and 71.2 MPa (COV = 27%). Interestingly, all specimens except specimen #4 failed on the back side of the sample first, and tensile failure stress from the front surface measurements were systematically higher in those cases. This likely comes from a bias in stress reconstruction as the crack propagates through the thickness or from bending. The tensile failure stress identifications had relatively high scatter (COV = 21-27%) compared to stiffness. While this is somewhat expected, the COV is notably higher than for reported quasi-static failure stress measurements (COV = 13% [31]), suggesting the scatter in the IBII test measurements is amplified by the varying level of three-dimensional loading in each test.

4.3.1 | Using reconstructed stress fields to detect through-thickness heterogeneity

As was shown in Sec. 4.2,bending deformation creates a bias in the reconstruction of average axial stress, which represents the first term on the right hand side of Eqs. (23) and (24). Therefore, a bias is expected to be present in the LSG reconstructions as well. However, an additional bias is expected in the linear term of Eqs. (23) and (24) since the surface accelerations ($a_x^{F,B}$, $a_y^{F,B}$) are used as an approximation for the membrane components of acceleration (a_x^o, a_y^o) in Eqs. (20) and (21). These two effects will be examined in the analysis that follows.

The maps of acceleration-based stress for the front and back surfaces (Eqs. (23) and (24)), and using back-to-back average fields (membrane component of stress only (Eq. (22)) for specimen #1 and #3 are shown in Figs. 10 and 11, respectively, at the time when a crack is first observed (occurs on the back face first for both samples). Also shown are the stress fields reconstructed from strains ($\sigma_{xx}(\epsilon_{xx})$ from Eq. (8)) and the difference between the two stress reconstructions. The location of fracture and virtual gauge used for extracting the failure stress is shown as a black rectangle in each figure.

Both specimens confirm the findings from Sec. 4.2 that back-to-back averaging can be used to reconstruct an unbiased estimate of the membrane stress (see Figs. 10g - 10i and Figs. 11g-11i). The acceleration-based stress fields reconstructed on the front and back faces are similar to each other when the crack first forms. These fields are also similar to the membrane stress field reconstructed using back-to-back average acceleration fields ($\sigma_{xx}^A(LSG)$ in Figs. 10 and 11). Considering Eqs. (20) and (21), this is not surprising since the stress associated with out-of-plane acceleration (a_z^o) cannot be resolved and therefore, Eqs. (23) and (24) reduce to a similar form to the membrane stress field (Eq. (22)). This explains why, on average, the failure stress identified from back-to-back averaged fields in Table 1 was similar to each face individually and with comparable scatter. Therefore, in the presence of out-of-plane loading, back-to-back averaging provides no benefit for failure stress estimation since only the membrane component of stress can be resolved.

The reconstruction bias is clear when comparing the acceleration and strain-based stress fields in Figs. 10 and 11. For example, at the onset of fracture the strain on the front surface of specimen #1 is compressive while the other face is tensile (Figs. 10a and 10d). This suggests there is an out-of-plane bending load superimposed on the axial loading. The same is shown for specimen #3, though the differences between the stress reconstructions on each face are smaller than for specimen #1. Since there is minimal variation in stress across the height of the sample at the onset of fracture, the agreement between the two stress reconstructions is largely dependent on the ability to reconstruct the average axial stress (first term on the right-hand side of Eqs. (23) and

(24)) using acceleration measurements from a single face. Based on Eqs. (20) and (21), this will only occur when out-of-plane acceleration (a_z^o) is minimal. However, these tests clearly show that this is not the case, and the out-of-plane effects lead to a significant bias in stress reconstructed from acceleration (for specimen #1: up to 70 MPa).

For these specimens, the bias from unresolved a_z^o stress is much larger than that caused by approximating membrane accelerations in the linear term of Eq. (22) with surface accelerations in Eqs. (23) and (24). This is demonstrated in Fig. 12 which shows stress fields reconstructed using the three-dimensional form of the linear stress-gauge (Eqs. (20)-(21), $\sigma_{xx}^{F,3D}$, $\sigma_{xx}^{B,3D}$) compared to the stress fields reconstructed using single-sided acceleration measurements (Eqs. (23)-(24)). For specimen #1, this bias is only present near the impact edge and is approximately one order of magnitude smaller than the differences measured between acceleration and strain-based stress reconstructions in Figs. 10 and 11.

It is possible to quantitatively compare full-field maps of stress reconstructed from acceleration and strain to assess the relevance of the assumption that loading is two-dimensional. Here we use the normalised RMS difference ($\tilde{d}_{RMS}$) calculated as:

$$\tilde{d}_{RMS}(t) = \frac{1}{|\hat{\overline{\sigma_{xx}(LSG)}}^{S}|}\sqrt{\frac{1}{N}\sum_{i=1}^{N}\left(\sigma_{xx}^{i}(LSG) - \sigma_{xx}^{i}(\epsilon_{xx})\right)^2} \tag{25}$$

from data collected only on the front face, to simulate an experiment where only one camera is used. In Eq. (25), N denotes the number of measurement points in the field of view at a given time, and $|\hat{\overline{\sigma_{xx}(LSG)}}^{S}|$ denotes the maximum, absolute value of the field-averaged stress reconstructed from the linear stress-gauge up to the point of fracture. It is also possible to generate a spatial map of the RMS difference ($\tilde{d}_{RMS}^{S}$) considering all time steps between the acceleration and strain-based stress reconstructions as:

$$\tilde{d}_{RMS}^{S}(x, y) = \frac{1}{|\hat{\overline{\sigma_{xx}(LSG)}}^{S}|}\sqrt{\frac{1}{M}\sum_{m=1}^{M}\left(\sigma_{xx}^{m}(LSG) - \sigma_{xx}^{m}(\epsilon_{xx})\right)^2} \tag{26}$$

where now the summation is performed for each pixel with respect to time, with M denoting the total number of frames before fracture. The temporal evolution of the RMS difference between the stress reconstructions for specimens #1 and #3 are shown in Fig. 13a. The normalised RMS error increases gradually for specimen #1 starting at 4 μs, followed by a rapid increase beyond 10 μs. This roughly corresponds to the point of wave rebound at the free edge. Similar trends are observed for specimen #3, but the normalised RMS difference is slightly lower towards the end of the test ($t > 15$ μs). This aligns with the analysis so far that shows out-of-plane loading effects are stronger in the case of specimen #1. Stress-strain curves in Fig. 8 and the temporal divergence of strain-based and acceleration-based stress in Fig. 14 can be used to infer that out-of-plane loading effects are minimal when the normalised RMS difference is less than approximately 0.1. For the spatial map of the RMS difference for specimen #1 (Fig. 13a), this implies that failure stress measurements are influenced by out-of-plane effects beyond approximately 7 mm from the free edge. These two diagnostics can be used to quickly assess if/when out-of-plane effects are significant, and when stress reconstructions from acceleration require careful interpretation.

4.3.2 | Diagnostics for detecting bias in fracture stress measurements from through-thickness heterogeneity

While the RMS difference between full-field stress reconstructions is useful for identifying when out-of-plane effects are present in the test, it is clear that the magnitude of the effect depend on position. Therefore, more careful consideration is required to assess if these effects are significant at the fracture location. Here we use the temporal evolution of stress within the virtual gauge area where the sample fractures, and the corresponding stress-strain curves from the virtual gauge.

From Figs. 14a and 14c it can be seen that the differences between strain-based and acceleration-based stress reconstructions at the fracture locations develop progressively starting near peak compressive load (approx. $t = 12\ \mu$s and for both specimens). At this point the stress-strain response between the two faces also diverged for specimen #1 (Fig. 14b). For specimen #3 (Fig. 14d) the stress-strain response on the front and back faces diverge at a slightly later time, and the magnitude of the divergence from strain-based stress is smaller (Fig. 14c), indicating out-of-plane effects are lower. We can associate the divergence of $\sigma_{xx}(LSG)$ and $\sigma_{xx}(\epsilon_{xx})$ for both specimens with a break down of the measurement assumptions, and not the constitutive model, since the stress-measures on each face agreed throughout much of the compressive loading sequence with the back-to-back averaged response. These diagnostics confirm that unresolved out-of-plane loading effects are significant at the fracture location on both samples and therefore, failure stress estimates will be biased. A more quantitative analysis of the bias will be performed in later sections with additional tests where three-dimensional effects are reduced.

4.4 | Back-to-back measurement summary

The back-to-back imaging experiments have resulted in the following key conclusions:

1. Measured strain fields showed a large back-to-back difference that builds over time and propagated from the impact edge into the sample.
2. The unloading response observed on the stress-strain curves produced with the stress-gauge equation was substantially different on each side of the sample. The differences were generally largest over the half of the sample closest to the impact edge.

3. Three-dimensional effects can have a significant influence on the identification of stiffness from a single side of a sample (up to 20% difference). However, the scatter is regularised by taking the average stiffness over the middle 50% of the sample. Over all tests, the modulus identified from single-sided measurements only differed by 3% compared to identifications made with the back-to-back averaged fields (see results in Table 1).

4. Three-dimensional effects were smallest near the free edge and therefore, scatter in stiffness measurements may be improved by refining the region on the sample used for spatial averaging. A large RMS variation (≥3%) of the spatial identification relative to the average over the middle 50% of the sample provides an indicator of when this refinement may be required.

5. Average failure stress obtained from each side of the sample were similar (see Table 1), but with relatively high scatter (COV = 20-27%). It was suspected that this was a result of varying levels of three-dimensional loading in each test.

6. Failure stress diagnostics provide evidence that most samples failed under combined in-plane tension and out-of-plane bending. While large differences in strain were measured between the two faces, the difference between in-plane accelerations were lower, and thus, the linear stress-gauge reconstructions were similar on each face. The out-of-plane component of acceleration generated under this loading strongly influenced the bias on failure stress. Since this out-of-plane component cannot be resolved, back-to-back measurements provide no benefit for failure stress estimation. Moreover, since this component is required to fully resolve axial stress (Sec. 2.3), stress reconstructions based on in-plane acceleration will underestimate the true failure stress. Unlike stiffness identifications, back-to-back measurements do not reduce the bias on failure stress. This is confirmed in later sections, when compared to tests where the effects of out-of-plane bending are reduced.

7. The full-field normalised RMS difference between acceleration and strain-based stress reconstructions may be used to quickly evaluate the relevance of the assumption that loading is two-dimensional. A normalised RMS difference above 0.1 was suggested as a rough guideline for establishing when out-of-plane loading effects become substantial.

Overall, in the presence of three-dimensional loading, back-to-back measurements provide more stable and consistent stiffness identification, but do not offer any improvement for failure stress. The remainder of this article will focus on three things: 1) identifying the source of this three-dimensional loading, 2) developing a method to correct it, and 3) performing a final series of experiments with significantly reduced through-thickness heterogeneity to quantify the effects on stiffness and failure stress measurements.

4.5 | Identifying the physical mechanisms behind the out-of-plane loading

The consistency of three-dimensional loading across all samples indicates that it was introduced systematically through the experimental setup. The most likely cause was angular misalignment in the impact chain. This was investigated with experiments where a mirror system was installed in the test chamber to visualise the out-of-plane impact alignment (Fig. 15).

Several test shots revealed that the waveguide was systematically misaligned to the projectile by 0.8°-1.2°. It is hypothesized that this misalignment arises from slight deviations in the barrel bore, which affects the flight of the short sabot (45 mm), but not the machined rod that sits deeper in the barrel when the alignment is performed. Images taken with the mirror system revealed that angular misalignment induces a bending wave in the waveguide leading to appreciable lateral displacement and rotation of the free end. This is apparent when comparing images taken before and after impact; two of which are overlaid in Fig. 16. When a sample was bonded to the back of the waveguide it was observed that the lateral motion introduced out-of-plane bending in the sample near the waveguide. Videos of these tests are included as supplementary material to this article.

These additional tests support the arguments that the pulse was applied non-uniformly through-the-thickness. As observed in the back-to-back imaging experiments (Sec. 4.2 & 4.3), the effect on the compressive loading decreases with increasing distance from the impact edge. This is believed to be a result of the Saint-Venant effect in dynamics, as reported by others [29, 30], which acts to even out the wave as it propagates away from the impact edge. The reason the three-dimensional effects amplify as the material unloads is a result of structural dynamics of the sample. Before the wave reaches the free edge, the specimen behaves like it is infinite in length. As the wave reflects from the free edge, the loading excites a bending mode in the sample, which propagates from the impact edge. The pulse length is also slightly longer than the length of the sample, and therefore, a type of 'forced' vibration is introduced until the specimen de-bonds from the waveguide. The effect of this bending wave is superimposed on the in-plane loading, as observed in the kinematic fields in Figs. 6-7.

Plotting the membrane components of stress and strain reveal the underlying linear-elastic response of the material (shown at four location in Fig. 17 and Fig. 18 for specimen #1 and #3, respectively), which can be used to identify the unbiased estimate of the interlaminar elastic modulus (Sec. 2.2). However, back-to-back measurements are unable to resolve the out-of-plane acceleration and thus, cannot fully resolve stress for the purposes of estimating failure stress in the presence of out-of-plane loading (see Eq. (19)). The 'flexural' stress-strain curves are shown Fig. 17e-17h and Fig. 18e-18h. Recall that the flexural components of strain and acceleration are computed using Eqs. (11)-(13). These stress-strain curves support that out-of-plane effects are significant, and flexural stress is clearly not well captured when the a_z^o component is neglected. Moreover, it can be said that the first term in Eq. (19) contributes little to the calculation of $\overline{\sigma_{xx}^{f}}^{y}$, since the stress-strain response diverges significantly from the back-to-back average response as otherwise, the responses would be linear for each face. This confirms that the true failure stress is underestimated using the linear stress-gauge reconstructions from each face when three-dimensional effects are present.

Note that in-plane displacement, and to a greater extent, in-plane strain measurements presented in the previous section contain some bias in proportion to the ratio of out-of-plane bending deformation to the camera stand-off distance. This effect could be obtained by finite element simulation of the misalignment, or by stereo digital image correlation. But even if this error could be quantified, the assumption of two-dimensionality would still be invalid. This provides compelling evidence for a need to improve the alignment procedure for further testing. The mirror system used for diagnostics (Fig. 15a) was used to implement a new alignment procedure which reduced the misalignment error to $\approx 0.2°$. The impact tests were then repeated with improved alignment to quantify the bias introduced by the three-dimensional loading on stiffness and failure stress measurements, as described in the following section.

5 | FOLLOW-UP EXPERIMENTS WITH IMPROVED ALIGNMENT

The alignment procedure in Sec 3.1 was extended to include additional test shots in the out-of-plane perspective to correct for yaw misalignment from the projectile trajectory. Using an image-based alignment process results in an angular and positional accuracy of 0.2° and 0.2 mm, respectively. The key steps are included in the Appendix of this article and the full details can be found in [25]. To quantify the effect of the improved alignment, eight impact tests with a single Shimadzu HPV-X camera were performed at impact speeds ranging from 25 $\mathrm{m{\cdot}s^{-1}}$ to 54 $\mathrm{m{\cdot}s^{-1}}$. The objective was to characterise: 1) the relative effect of improving the alignment on stiffness and failure stress measurements, and 2) the response of the material under varied impact speeds where the specimen fails and does not fail. When combined with the back-to-back imaging experiments, the intention was also to establish a set of diagnostics for detecting three-dimensional effects from single-sided measurements. This has considerable practical benefit as most users will only have access to one camera.

5.1 | Reconstructed stress-strain response and stiffness identification

The stress-strain curves at four locations for a sample impacted at 25 $\mathrm{m{\cdot}s^{-1}}$ (R7), 35 $\mathrm{m{\cdot}s^{-1}}$ (R6) and 50 $\mathrm{m{\cdot}s^{-1}}$ (R4) are shown in Fig. 19. Note that stress and strain are computed from acceleration and strain fields assuming two-dimensionality (*i.e.:* no decomposition into membrane and flexural components). The stiffness and failure stress measured for each sample are included in Table 2. The spatial identifications of E_{33} for all samples are shown in Fig. 20. Note that the identification of E_{33} in Table 2 was determined by fitting the compressive stress-strain response up to 8 $\mathrm{mm{\cdot}m^{-1}}$, for consistency with the previous tests. Specimens tested with the revised alignment procedure are denoted by ‘R’ preceding the specimen number.

An impact speed of 25 m·s^{-1} (specimen R7) was selected to quantify the effect of improving the alignment on the stress-strain response under conditions where material damage can be ruled out. The stress-strain curves for this sample are shown in sub figures (a)-(d) in Fig. 19. These measurements verify the expected linear-elastic behaviour of the material, with negligible spatial variation in the unloading behaviour, unlike that measured in the first set of tests (recall Fig. 8). As the impact speed is increased to 35 m·s^{-1}, the unloading portion of the stress-strain curves at $x/L = 0.67$ (Fig. 19g) and 0.83 (Fig. 19h) differs from the loading behaviour and some parasitic non-linearity is measured near peak compressive load. This unloading divergence becomes more pronounced as impact speed increases (Fig. 19k-19l). It is speculated that this is a result of weakly activated bending modes caused by residual misalignment of the waveguide, or of the sample. The non-linearity observed in the curves is not a material behaviour, since its onset is dependent on spatial location and not stress. For example, non-linear behaviour is observed below 150 MPa near the impact edge at 35 m·s^{-1} (Fig. 19h), but is not observed near the free edge at 50 m·s^{-1} where stresses exceed 150 MPa (Fig. 19j).

The effect of improved alignment is apparent in the stiffness measurements, where spatial identifications were much more stable (Fig. 20) over all tests (Table 2). Despite some lingering three-dimensional effects in the stress-strain curves, the RMS variation of all spatial identifications was reduced (all tests lower than 3%, and most lower than 2%). Furthermore, when the alignment was improved the average stiffness from all tests was within one standard deviation of that identified from the membrane components of stress and strain using back-to-back averaging. This provides additional confidence that the identifications from tests with improved alignment were unbiased by 3D effects over most of the sample up to 8 mm·m^{-1} of strain.

5.2 | Failure stress identification

Here we will consider specimen R7 (25 m·s^{-1}) and specimen R4 (50 m·s^{-1}), to investigate how impact speed and residual misalignment influence stress reconstructions. It is worth noting that sample R7 did not fracture so $\sigma_{xx}(LSG)$ and $\sigma_{xx}(\epsilon_{xx})$ should agree throughout the whole test. The failure stress diagnostics from Section 4.3 are presented for specimen R7 and R4 in Fig. 21 and Fig. 22, respectively. In Fig. 22, two virtual gauge regions are considered to compare the response at the location of fracture, and at $x/L = 0.67$ where the average stress-strain curve shows a dissimilar unloading behaviour.

The failure stress diagnostics for specimen R7 (Fig. 21) show a good agreement between the stress reconstructed from strain, and from the linear stress-gauge equation. Average stresses within a virtual gauge in the centre of the sample agree well over the entire test (Fig. 21c) and the material response is linear elastic during loading and unloading (Fig. 21d). This validates the assumed constitutive model and implies that the loading remains two-dimensional throughout the entire test in this region of the sample.

For sample R4 impacted at 50 m·s^{-1}, the two stress maps, and temporal evolution of stress within the virtual gauge at the point of fracture are also in good qualitative agreement until the crack forms. At this point, the strains become non-physical and the strain-based stress diverges (Fig. 22c). Similar to sample R7, tested at 25 m·s^{-1}, the stress-strain curve at the crack location (Fig. 22d) is linear up to fracture, with no sign of three-dimensional effects on the unloading response.

The effects of misalignment are detected in sample R4 closer to the impact edge, as demonstrated using the stress and strain reconstructed with a virtual gauge at $x/L = 0.67$. In the centre of the sample the linear stress-gauge reduces to the average stress-gauge equation (Eq. 3), but is used here to show how the stress-strain response in Fig. 19k directly compares to stress reconstructed from strain. In a similar manner to the back-to-back imaging tests, the two stress reconstructions start to diverge near peak compressive load (Fig. 22e). At this time in the test it is believed that structural bending has propagated to this location. As discussed previously, it is most likely that the offset occurs because of a bending wave. Section 4.3 showed that the bending wave was captured in surface strain measurements, but was not captured in surface accelerations since bending stress is primarily a function of out-of-plane acceleration, which cannot be resolved. However, in this case, the offset is much smaller than in previous tests (see Fig. 14), and the region over which three-dimensional effects are witnessed does not reach the fracture location.

The improvement in alignment is also shown across all specimens in a substantial reduction in the temporal RMS difference between the acceleration and strain-based stress fields over the entire test (see Fig. 23). The normalised RMS difference was low (approx. 0.05) during the initial compressive loading for all samples, indicating that the stiffness was not likely to be affected. This is supported by the improved spatial stability of the interlaminar stiffness identified using stress-strain curves, low measurement scatter across all samples, and good agreement with the unbiased estimates of stiffness using back-to-back averaging from Sec. 4.2. However, the RMS difference still increases over the second half of the test, and using the previously proposed threshold of 0.1 would suggests that some out-of-plane loading may be present and failure stress estimates may require more careful consideration.

The full-field map of the RMS difference in Fig. 24 provides valuable insight into where the out-of-plane effects are significant. The RMS difference map for specimen R4 shows a similar distribution to specimen #1 presented in Fig. 13b, with larger RMS difference over the half of the specimen closest to the impact edge. However, the magnitude of the difference is dramatically reduced overall, confirming that improved alignment reduces the out-of-plane effects. Using the same RMS difference threshold of 0.1 it can be inferred that out-of plane effects only become significant for cross sections located further than 10 mm from the free edge, and are negligible over the sample where fracture occurs (shown by black rectangle in Fig. 24). Note that the RMS difference also increases near the free edge where data is reconstructed ($x < 1$ mm) and where grid defects are present (circular spots of $\tilde{d}_{RMS} \approx .\ 0.1$ at $y = 3$ mm). The agreement between the stress measures shown in Fig. 22d and low RMS difference over the field where fracture occurs gives confidence in the identified failure stress for this sample of 95 MPa. This represents a nearly 30% increase compared to measurements made under the effect of three-dimensional loading (recall results in Table 1).

Comparing these revised alignment tests to the previous back-to-back experiments shows that the three-dimensional effects cause failure stress to be underestimated by at least 30%. Under improved alignment conditions, the average failure stress was 104 MPa and measurement consistency was dramatically improved (COV < 7%) as listed in Table 2. This level of consistency is remarkable given that the strain rates are on the order of 5×10^3-$1\times10^4 s^{-1}$. This is significantly lower than the reported scatter in the previous study by the authors (COV = 21% [15]) and the quasi-static characterisation (COV = 13% [31]). These results highlight the importance of test alignment for failure stress measurements.

6 | DISCUSSION

The synchronised front and back measurements and follow-up experiments with a single-camera have revealed a number of diagnostic features to help identify cases where measurement assumptions of the IBII test begin to break down. Some recommendations for future test design can be drawn from these results. These key findings and recommendations from this study are summarised below.

1) Single-sided failure stress diagnostics provide an excellent indication of when the loading becomes three-dimensional. In the current tests this appeared as a divergence between stress and strain after the wave reflects. If this is observed in measurements at the fracture location, the failure stress needs to be interpreted with caution as it could be underestimated by at least 30%. Moreover, a normalised RMS difference greater than 0.2 between acceleration and strain-based stress reconstructions can also be used to quickly assess if/when out-of-plane effects are significant, and when stress reconstructions from acceleration require careful interpretation.

2) Three-dimensional effects can also be detected in the average stress-strain curves by unloading that differs dramatically from the loading behaviour. It also appeared as a spatial dependence on the stress-strain response and stiffness identification, when the material was not expected to have significant heterogeneity. In this work, misalignment was found to have a small influence on average stiffness measured over multiple tests. While the bias can be large for a single sample when alignment is poor (up to 7%), over several samples the bias was at most 4%. When three-dimensional loading is an issue, the bias in stiffness measurements may be reduced by weighting the spatial average of the stiffness identification towards the free edge where the effects are lower. A high RMS variation (≥ 3%) of the spatial identification relative to the mean over the middle 50% can be used as an indication of when this may be needed.

3) Misalignment in the impact chain is an important problem to consider in future test design and establishing tolerances on experimental alignment. If one has the flexibility to machine longer samples (*e.g.:* for in-plane testing), the Saint-Venant effect can be better exploited by measuring the behaviour only over the region of the sample where three-dimensional effects are minimal. In the case of the interlaminar tests where the length is limited, it is important to design the test such that fracture occurs nearer to the free-edge, and that alignment is as good as possible to enable more of the sample to be used for stiffness identification. With the new alignment procedure it was possible to make unbiased measurements over approximately half of the sample ($x < 10$ mm). The issue of alignment is particularly important in other IBII tests on brittle materials where out-of-plane bending can significantly influence measured properties (*i.e.*: ceramics, concrete, *etc.*).

7 | FUTURE WORK

With the alignment improved, it may now be possible to investigate 'secondary effects' that may contribute to the residual three-dimensional loading. These include: specimen manufacturing quality (edge squareness) and alignment on the waveguide, the type of glue used to bond the specimen to the waveguide, and sample thickness. The most prominent secondary effect is the alignment of the sample on the waveguide, as this may interact with the projectile misalignment to amplify the three-dimensional loading. This could be studied by simulating the impact with a 3D model, and validating by experiments with intentional misalignment. More rigorous alignment procedures could be developed to reduce, and better control the waveguide angular misalignment. As shown in the follow-up experiments, improved angular alignment reduces bending deformation and thus allows more of the sample to be used reliably for stiffness and failure stress identification. Alternative impact arrangements may also be considered to expedite the alignment and reduce variability in the positioning of the waveguide. It would be beneficial to increase the length of the waveguide to allow more time for the wave to even out before entering the sample. This could be combined with an alternative arrangement where impact occurs nearer to the barrel exit to reduce variability in projectile flight.

8 | CONCLUSIONS

As part of ongoing development of the image-based inertial impact (IBII) tests, it was important to understand the limitations of the experimental setup and validity of the two-dimensional assumption required to use full-filed measurements for material characterisation. Using two synchronised, ultra-high-speed cameras combined with full-field measurements from both sides of the sample, it was possible to identify cases where the assumption of uniform through-thickness behaviour was not satisfied. To the authors' knowledge, this is the first time such a study has been performed in dynamics. The key results from this study are summarised below:

- Results show that when the waveguide and projectile were misaligned between 0.8-1.2°, a bending wave was introduced into the sample after the wave reached the free edge. This non-uniform loading through-the-thickness was shown to have a substantial effect on stiffness identified from individual tests (difference between faces up to 20%), but a lesser effect over several samples (difference between average identifications was at most 4%, with COV = 3-4%).

- A mirror system in the capture chamber was used to extend the alignment procedure to account for out-of-plane misalignments to within 0.2°.

- Follow-up experiments with a single camera showed a significant improvement in consistency for measurements of the interlaminar stiffness and failure stress at strain rates on the order of 3,000 s^{-1}. Scatter on interlaminar failure stress measurements (COV = 7%) were much improved compared to the previous study by the authors (21%, respectively) [15], which highlights the importance of two-dimensional loading for accurate failure stress measurements.

- Comparison of these experiments to tests with back-to-back measurements allowed us to estimate the bias introduced by the three-dimensional loading on stiffness and failure stress measurements. The identification of stiffness under three-dimensional loading was biased by 4% at most on average. The effect on failure stress was much larger as the bending stress was not captured by the linear stress-gauge reconstructions on each face, causing failure stress to be underestimated by 30% on average.

- The two sets of experiments under different amounts of misalignment were useful in establishing diagnostics for detecting issues with three-dimensional loading from single-sided measurements. This included analysis of the unloading behaviour of the stress-strain curves along the sample, and a divergence of stress reconstructed from strain and acceleration in the failure stress diagnostics.

This study has demonstrated the importance of impact alignment for reliable characterisation of the interlaminar failure stress. This also improves the consistency of stiffness measurements, which are made at strain rates that are not achievable with existing test methods (on the order of 3-5,000 s^{-1}). The outcomes of this work will support efforts to design tests for obtaining failure stress measurements under combined tension/shear loading and begin populating failure envelopes at high strain rates. This information is not currently available at the strain rates considered here, and would be an invaluable advancement for improved high strain rate modelling of composite materials.

ACKNOWLEDGEMENTS

This material is based on research sponsored by the Air Force Research Laboratory, under agreement number FA9550-17-1-0133. The authors are grateful to the grant programme manager, Dr. David Garner from EOARD/AFOSR. The U.S. Government is authorized to reproduce and distribute reprints for Governmental purposes notwithstanding any copyright notation thereon. The views and conclusions contained herein are those of the authors and should not be interpreted as necessarily representing the official policies or endorsements, either expressed or implied, of the Air Force Research Laboratory or the U.S. Government. The authors kindly acknowledge Dr. Devlin Hayduke from Material Sciences Corporation, USA for supplying the material tested in this work. The authors would like to thank Sam Parry and Xavier Régal for their technical assistance in performing the experiments. Dr. Lloyd Fletcher and Prof. Fabrice Pierron acknowledge support from EPSRC through grant EP/L026910/1. Jared Van Blitterswyk acknowledges PhD funding support from EPSRC.

DATA PROVISION

All data supporting this study are openly available from the University of Southampton repository at: https://doi.org/10.5258/SOTON/D1093.

References

[1] R. Gerlach, C.R. Siviour, N. Petrinic, J. Wiegand, *Polymer* **2008**, 49(11), 2728-2737.

[2] J. Van Blitterswyk, L. Fletcher, F. Pierron, *Advanced Experimental Mechanics* **2017**, 2, 3-28.

[3] R. Olsson, *Composites Science and Technology* **2011**, 71(6), 773-783.

[4] W. Chen, *Journal of Dynamic Behaviour of Materials* **2016**, 2, 2-14.

[5] Z. Li, J. Lambros, *Composites Science and Technology* **1999**, 59, 1097-1107.

[6] T. Yokoyama, K. Nakai, *SEM X International Congress & Exposition on Experimental & Applied Mechanics* **2004**, 1-8.

[7] G. III Grey, *Mechanical testing and evaluation, ASM Handbook*, Vol. 8, 462-476, ASM International, **2000**.

[8] B.A. Gama, S. Lopatnikov, J.W. Gillespie Jr., *Applied Mechanics Reviews* **2004**, 57(4), 223-250.

[9] R. Moulart, F. Pierron, S.R. Hallet, M.R. Wisnom, *Experimental Mechanics* **2011**, 51(4), 509-536.

[10] F. Pierron, P. Forquin, *Strain* **2012**, 48(5), 388-405.

[11] F. Pierron, H. Zhu, C.R. Siviour, *Philosophical Transactions of the Royal Society A* **2014**, 372, 20130195.

[12] B. Koohbor, A. Kidane, W.-Y. Lu, M.A. Sutton, *International Journal of Impact Engineering* **2016**, 91, 170-182.

[13] L. Fletcher, J. Van Blitterswyk, F. Pierron, *EPJ Web of Conferences, DYMAT* **2018**, 183, 02041.

[14] L. Fletcher, J. Van Blitterswyk, F. Pierron, *Journal of Dynamic Behavior of Materials* **2019**, 5, 65-92.

[15] J. Van Blitterswyk, L. Fletcher, F. Pierron, *Journal of Dynamic Behavior of Materials* **2018**, 4, 543-572.

[16] L. Fletcher, F. Pierron, *Journal of Dynamic Behavior of Materials* **2018**, 4, 481-504.

[17] S.H. Yoon, M. Winters, C.R. Siviour, *Experimental Mechanics* **2016**, 56(1), 25-35.

[18] S.H. Yoon, C.R. Siviour, *Journal of Dynamic Behavior of Materials* **2017**, 3(1), 12-22.

[19] P. Forquin, B. Lukić, *Journal of Dynamic Behavior of Materials* **2018**, 4, 34-55.

[20] B. Lukić, D. Saletti, P. Forquin, *Journal of Dynamic Behavior of Materials* **2018**, 4, 56-73.

[21] F. Pierron, M. Grédiac, *The virtual fields method: extracting constitutive mechanical parameters from full-field deformation measurements*, Springer, Berlin, **2012**.

[22] F. Pierron, *Journal of Composite Materials* **1998**, 32(22), 1986-2015.

[23] Y. Surrel, *The grid method (GM)*, http://photodyn.org/wp-content/uploads/2016/ 03/Report_UniversityPrintCentre.pdf, **2018**.

[24] Y. Surrel, *The grid method (GM)*, http://photodyn.org/wp-content/uploads/2016/ 03/Report_UniversityPrintCentre_2.pdf, **2018**.

[25] L. Fletcher, J. Van Blitterswyk, F. Pierron, *A manual for conducting image-based inertial impact (IBII) tests*, https://doi.org/10.5258/SOTON/P0015, **2019**.

[26] M. Rossi, F. Pierron, *International Journal of Solids and Structures* **2012**, 49, 420-435.

[27] B. Lukić, P. Forquin, *Philosophical Transactions of the Royal Society A* **2017**, 375, 20160168.

[28] F. Pierron, F. Cerisier, M. Grédiac, *Journal of Composite Materials* **2000**, 34(12), 1028-1054.

[29] F. Zhu, F. Pierron, *Experimental Mechanics* **2016**, 56(1), 3-23.

[30] B. Karp, D. Durban, *Applied Mechanics Reviews* **2011**, 64(2), 020801.

[31] E. Clarkson, T. Valliappan, D. Tan, *CYTEC (Formerly Advanced Composites Group) MTM45-1/ 12K AS4 145gsm 32%RW Unidirectional Qualification Statistical Analysis Report FAA Special Project Number SP3505WI-Q Test Panel Fabrication Facility*, **2016**.

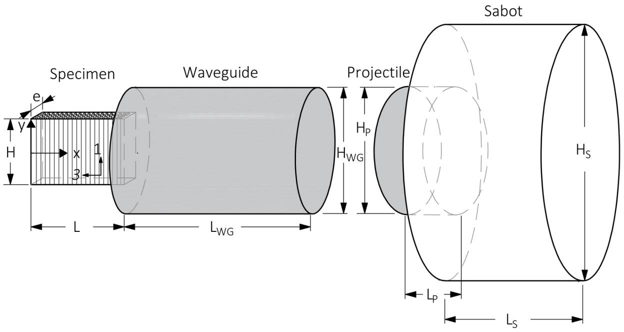

FIGURE 1 Schematic of the interlaminar IBII test

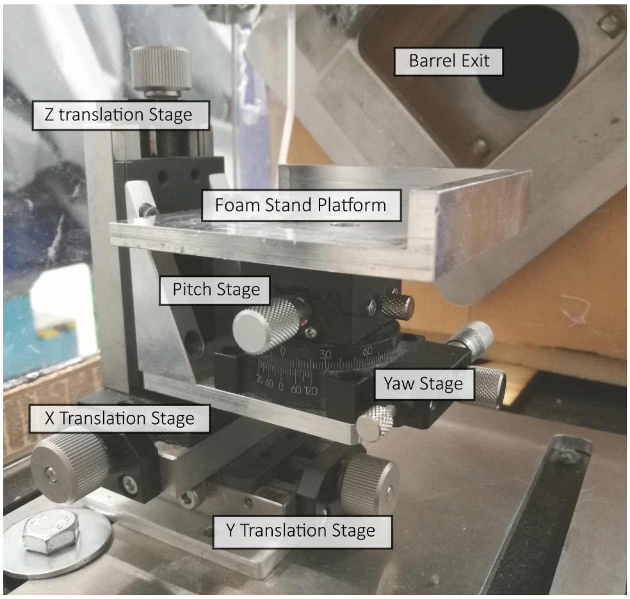

FIGURE 2 New 5-axis waveguide alignment stand (translational degrees of freedom in x, y and z, and rotational degrees of freedom in pitch and yaw)

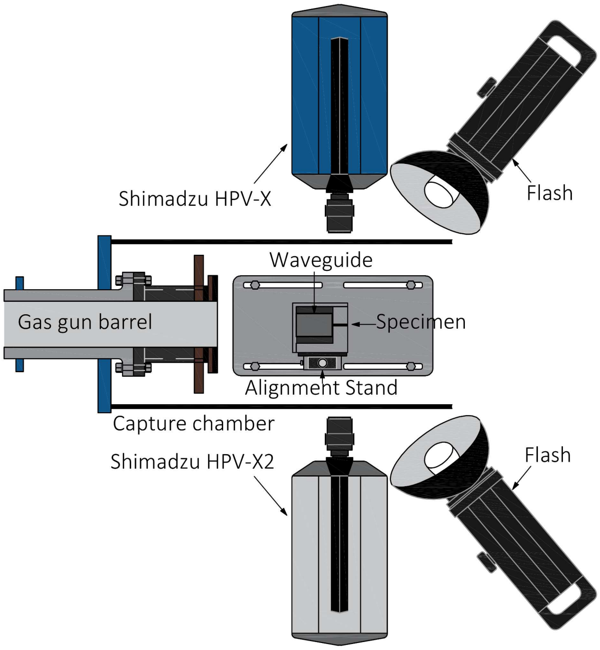

FIGURE 3 Schematic of the experimental multi-camera configuration

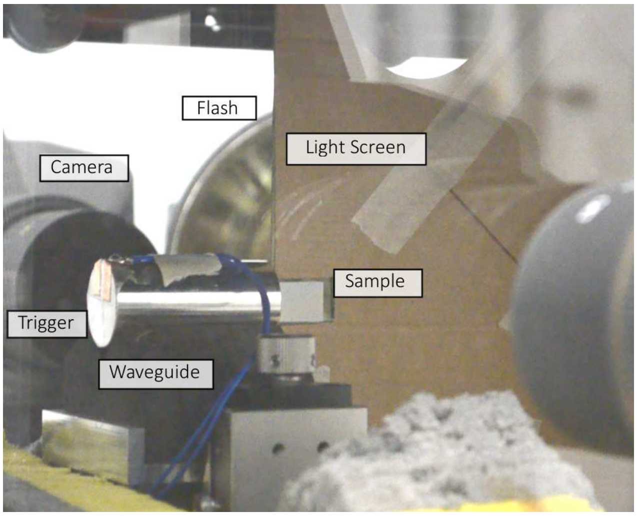

FIGURE 4 Light screen installed in the test chamber to allow for independent control of light intensity and uniformity on each side of the sample

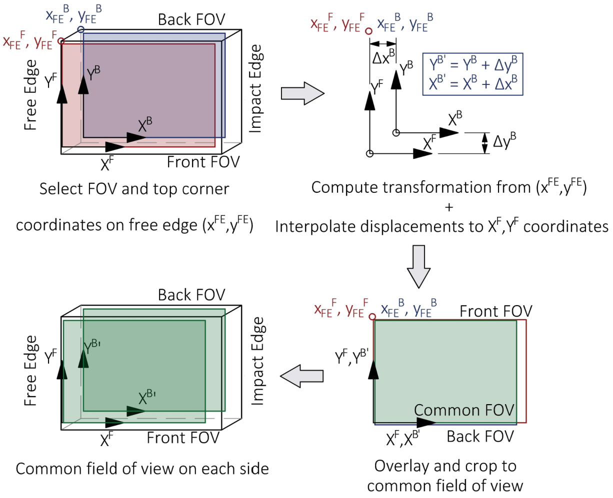

FIGURE 5 Procedure for transforming back face displacement fields to front face coordinates

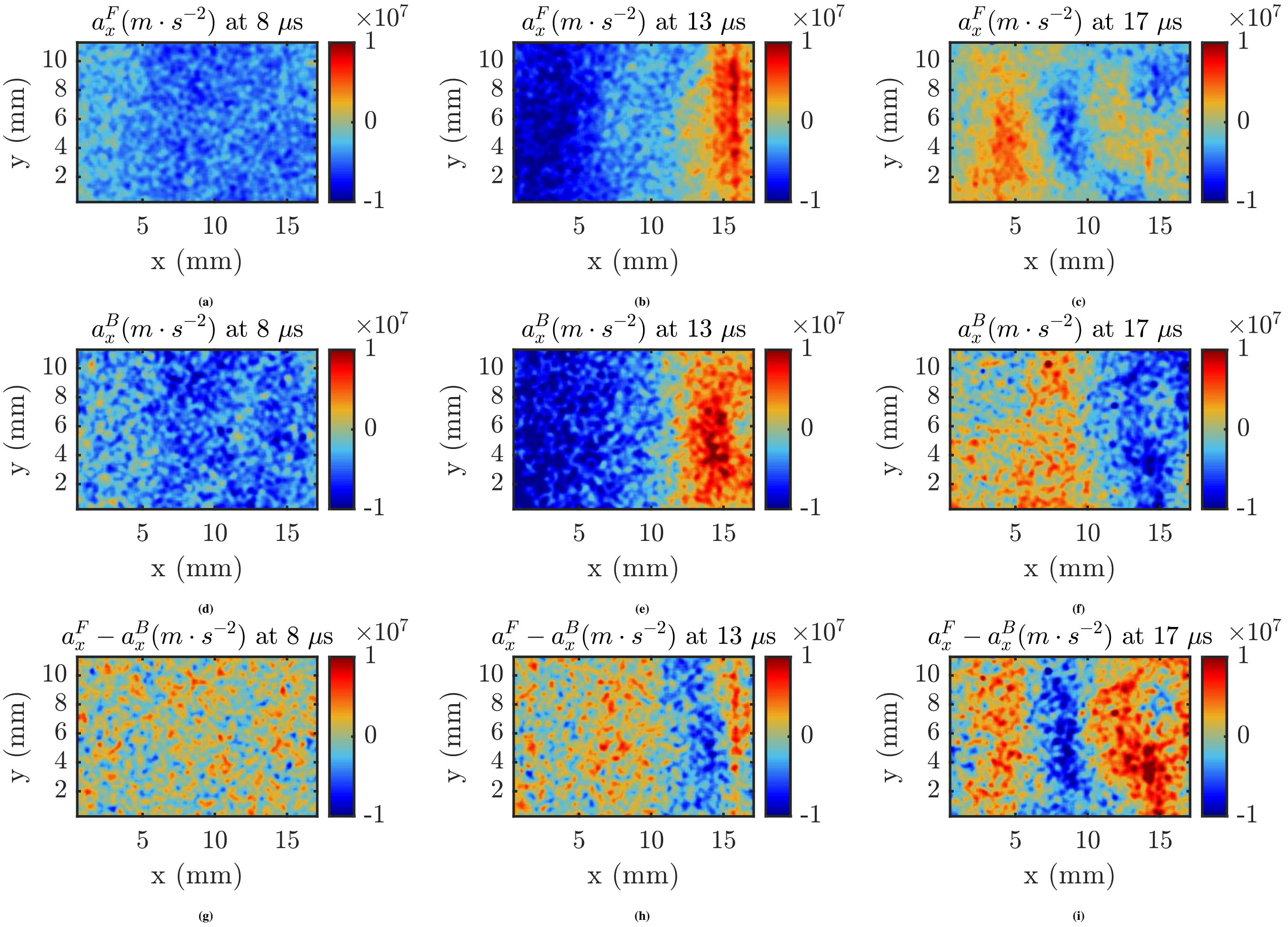

(a) (b) (c)

(d) (e) (f)

(g) (h) (i)

FIGURE 6 Acceleration (a_x) fields for specimen #1 measured on the front and back faces of the sample at three time steps and the difference between the two fields at each time step

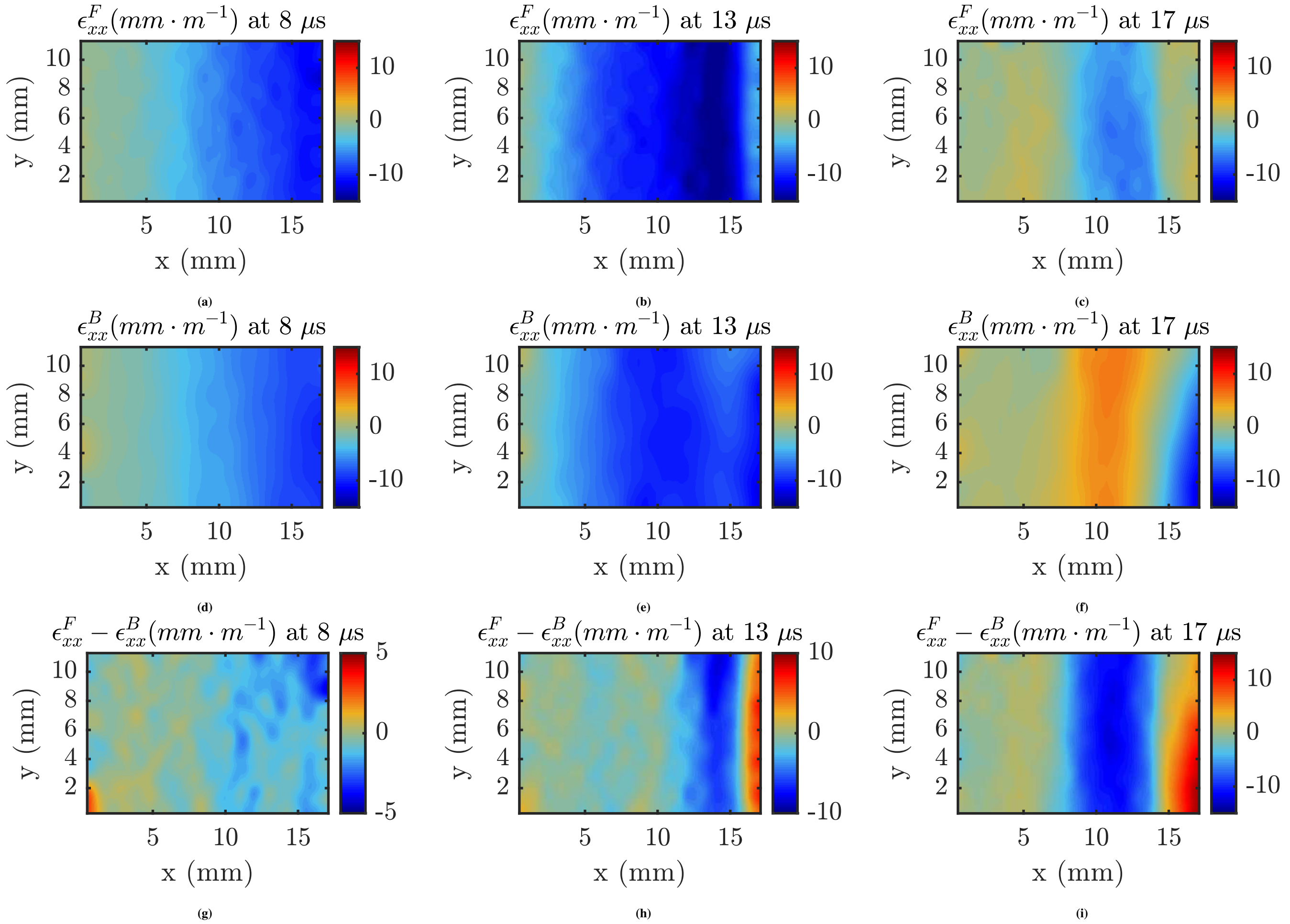

FIGURE 7 Strain (ϵ_{xx}) fields for specimen #1 measured on the front and back faces of the sample at three time steps and the difference between the two fields at each time step

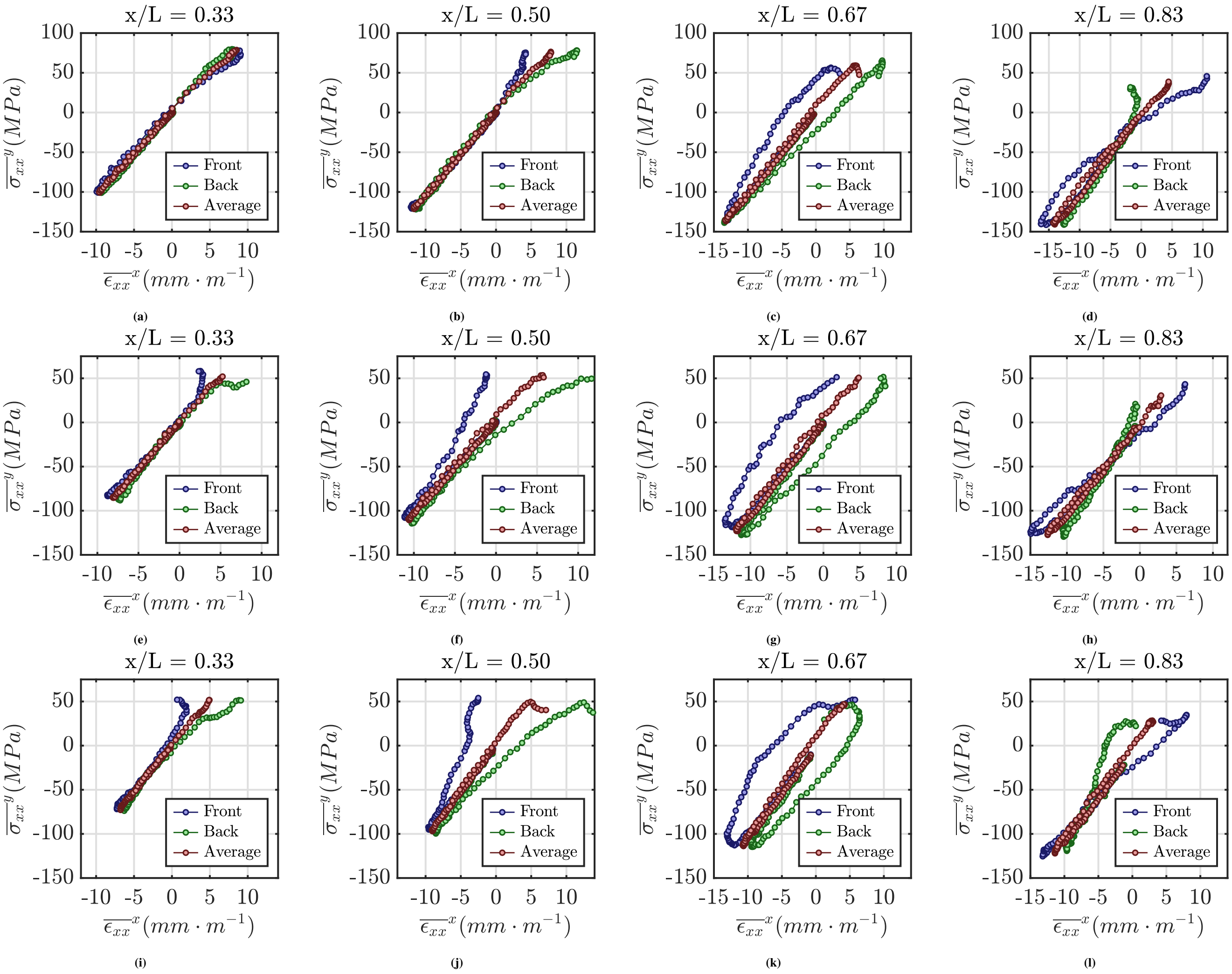

FIGURE 8 Stress-strain curves for specimen #3 ((a)-(d)), #1 ((e)-(h)) and #5 ((i)-(l)) as reconstructed with the stress-gauge equation using fields measured on the front and back faces independently, as well as assuming a linear through-thickness distribution between the two surface measurements (back-to-back averaging)

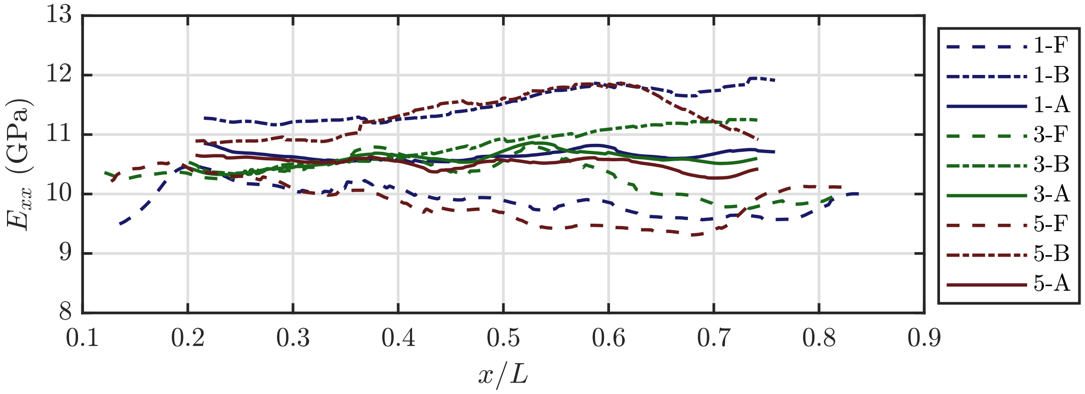

FIGURE 9 Interlaminar Young's modulus, E_{33}, identified from stress-strain curves reconstructed with the stress-gauge equation and average axial strain up to 8 mm·m^{-1} for specimens #1, 3 and 5. Note that 'F', 'B' 'A' denote the front and back faces, and back-to-back averaging, respectively

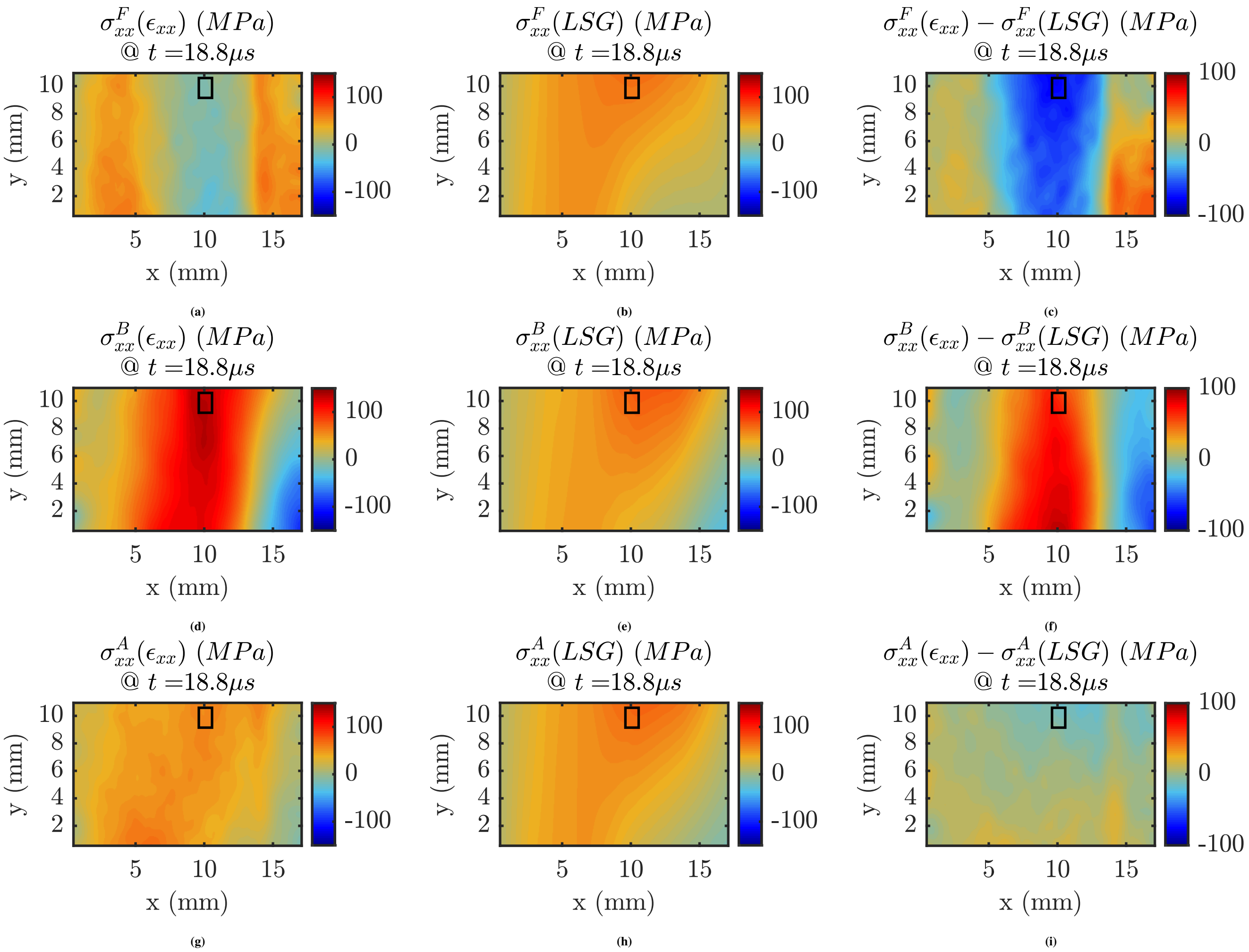

FIGURE 10 Failure stress identification diagnostics for specimen #1 at $t = 18.8$ μs corresponding to the frame of maximum tensile stress on the back face when the crack first appears: (a) strain-based stress field (MPa) constructed from ϵ_{xx}, using identified E_{33} from the front face ($\sigma^F_{xx}(\epsilon_{xx})$), (b) acceleration-based stress field (MPa) reconstructed using the linear stress-gauge equation on the front face ($\sigma^F_{xx}(LSG)$), (c) difference between strain-based and acceleration-based stress fields on the front face, (d) strain-based stress field (MPa) from the back face ($\sigma^B_{xx}(\epsilon_{xx})$), (e) acceleration-based stress field (MPa) on the back face ($\sigma^B_{xx}(LSG)$), (f) difference between strain-based and acceleration-based stress fields on the back face, (g) strain-based membrane stress field from back-to-back averaging (MPa) ($\sigma^A_{xx}(\epsilon_{xx})$), (h) acceleration-based membrane stress field from back-to-back averaging (MPa) ($\sigma^A_{xx}(LSG)$), (i) difference between strain-based and acceleration-based membrane stress fields. Note that the virtual gauge is shown as a black rectangle

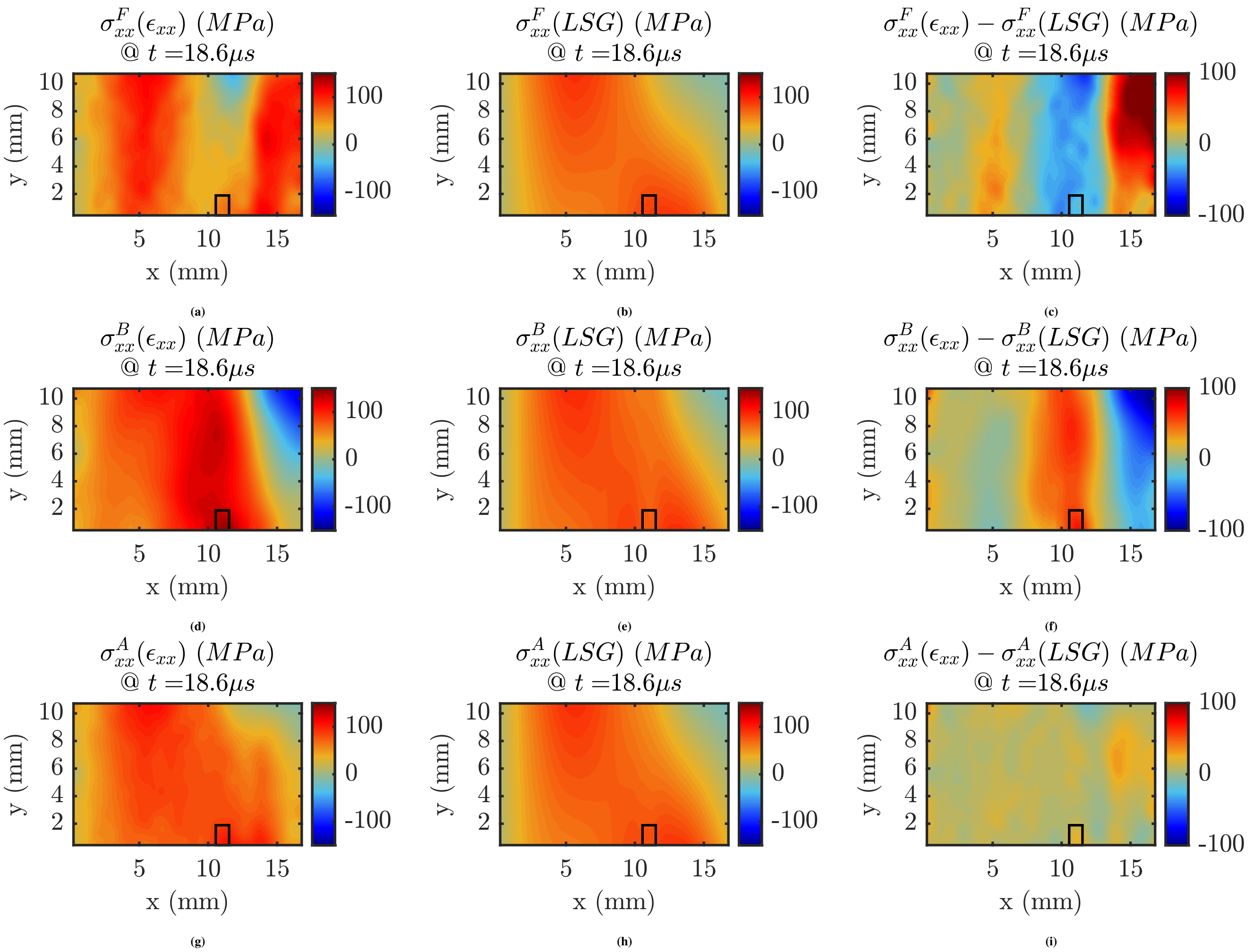

(a) (b) (c) (d) (e) (f) (g) (h) (i)

FIGURE 11 Failure stress identification diagnostics for specimen #3 at $t = 18.6$ μs corresponding to the frame of maximum tensile stress on the back face when the crack first appears: (a) strain-based stress field (MPa) constructed from ϵ_{xx}, using identified E_{33} from the front face ($\sigma^F_{xx}(\epsilon_{xx})$), (b) acceleration-based stress field (MPa) reconstructed using the linear stress-gauge equation on the front face ($\sigma^F_{xx}(LSG)$), (c) difference between strain-based and acceleration-based stress fields on the front face, (d) strain-based stress field (MPa) from the back face ($\sigma^B_{xx}(\epsilon_{xx})$), (e) acceleration-based stress field (MPa) on the back face ($\sigma^B_{xx}(LSG)$), (f) difference between strain-based and acceleration-based stress fields on the back face, (g) strain-based membrane stress field from back-to-back averaging (MPa) ($\sigma^A_{xx}(\epsilon_{xx})$), (h) acceleration-based membrane stress field from back-to-back averaging (MPa) ($\sigma^A_{xx}(LSG)$), (i) difference between strain-based and acceleration-based membrane stress fields. Note that the virtual gauge is shown as a black rectangle

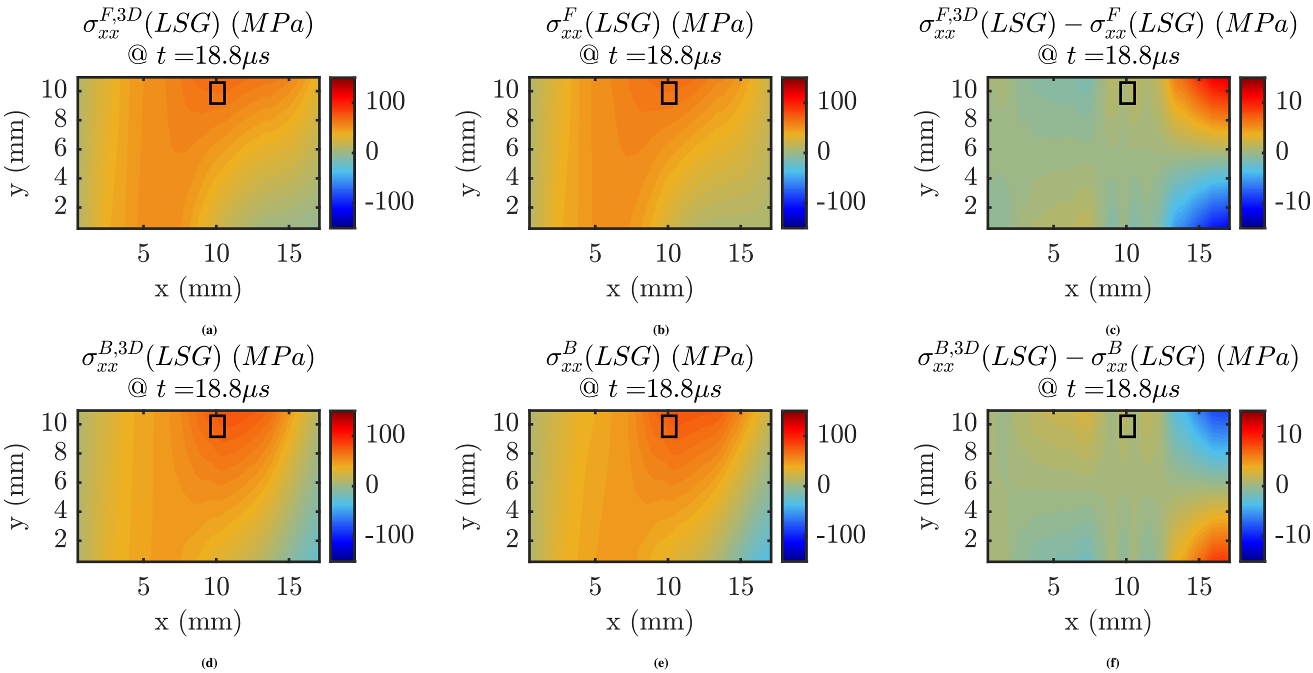

(a) (b) (c)

(d) (e) (f)

FIGURE 12 Comparison of acceleration-based stress reconstructions for specimen #1 at $t = 18.8$ μs corresponding to the frame of maximum tensile stress on the back face when the crack first appears: (a) acceleration-based stress field (MPa) on the front face using back-to-back measurements to evaluate Eq. (20) ($\sigma_{xx}^{F,3D}(LSG)$), (b) acceleration-based stress field (MPa) on the front face using single-sided measurements to evaluate Eq. (23) ($\sigma_{xx}^{F}(LSG)$), (c) difference between acceleration-based stress fields on the front face, (d) acceleration-based stress field (MPa) on the back face using back-to-back measurements to evaluate Eq. (20) ($\sigma_{xx}^{B,3D}(LSG)$), (b) acceleration-based stress field (MPa) on the back face using single-sided measurements to evaluate Eq. (24) ($\sigma_{xx}^{B}(LSG)$), (c) difference between acceleration-based stress fields on the back face. Note that the virtual gauge is shown as a black rectangle

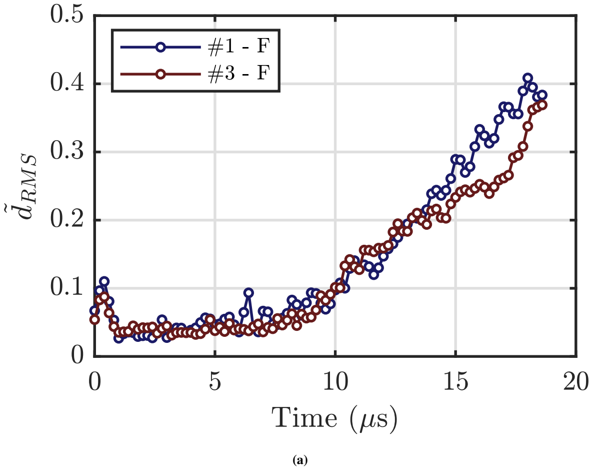

(a)

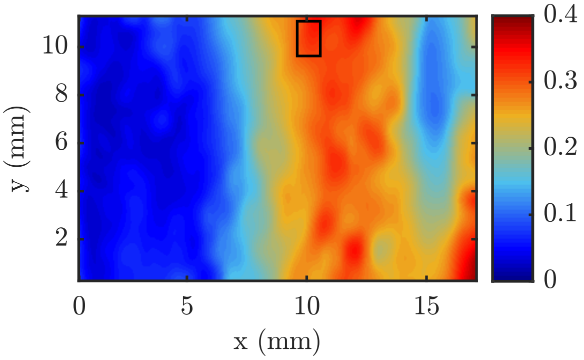

(b)

FIGURE 13 Failure stress diagnostics based on normalised RMS differences between acceleration and strain-based stress reconstructions (a) temporal evolution of the normalised RMS difference between acceleration and strain-based stress reconstructions on the front surface of specimen #1 and #3, and (b) spatial variation in RMS difference considering all time steps up to fracture. Note that the temporal normalised RMS difference increases later in the test as out-of-plane loading effects become more significant, and that the black rectangle in (b) denotes the virtual gauge centred on the location of fracture

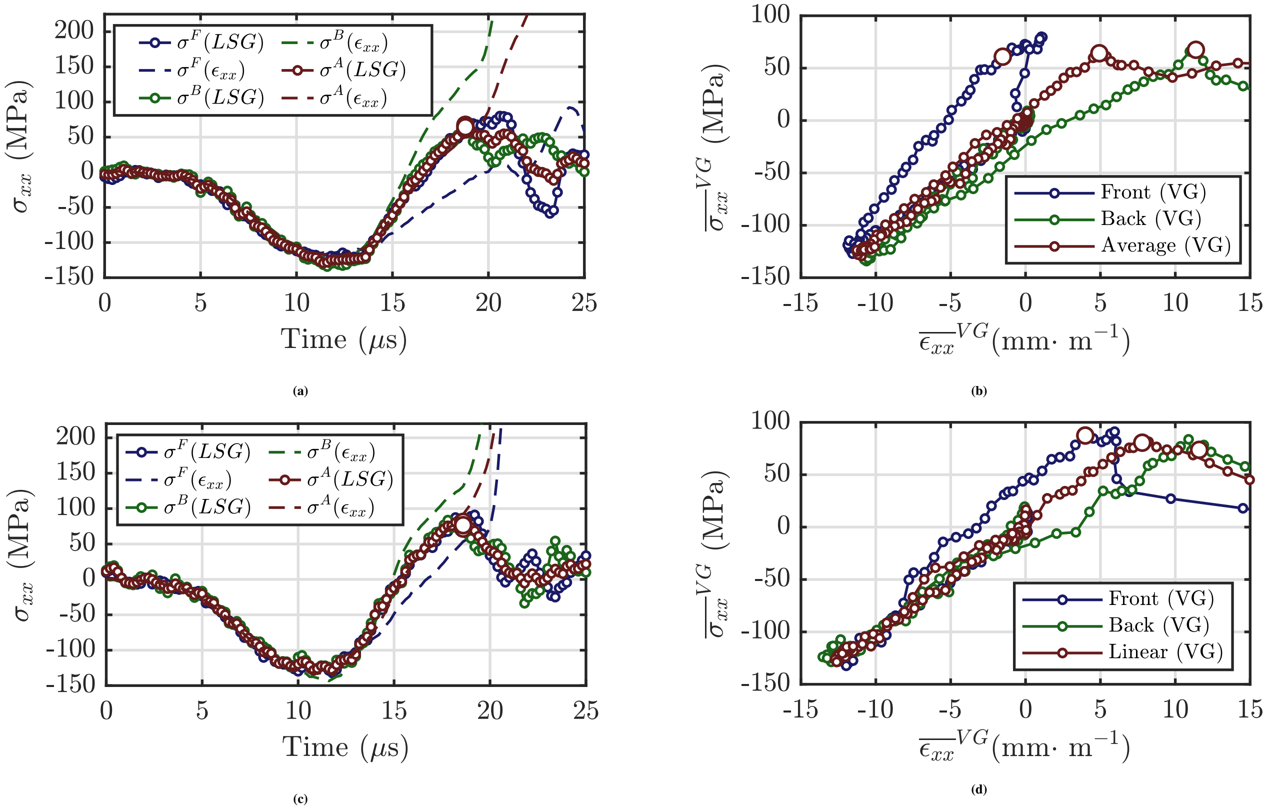

(a)

(b)

(c)

(d)

FIGURE 14 Failure stress diagnostics for specimen #1 and #3 showing: (a,c) comparisons of stress over time within the virtual gauge, (b,d) comparisons of stress-strain curves reconstructed using average stress (linear stress-gauge) and strain within the virtual gauge. Sub figures (a) and (b) correspond to specimen #1, and (c) and (d) correspond to specimen #3. Note that ’F’, ’B’ ’A’ in (a) denote the front and back faces, and back-to-back averaging, respectively

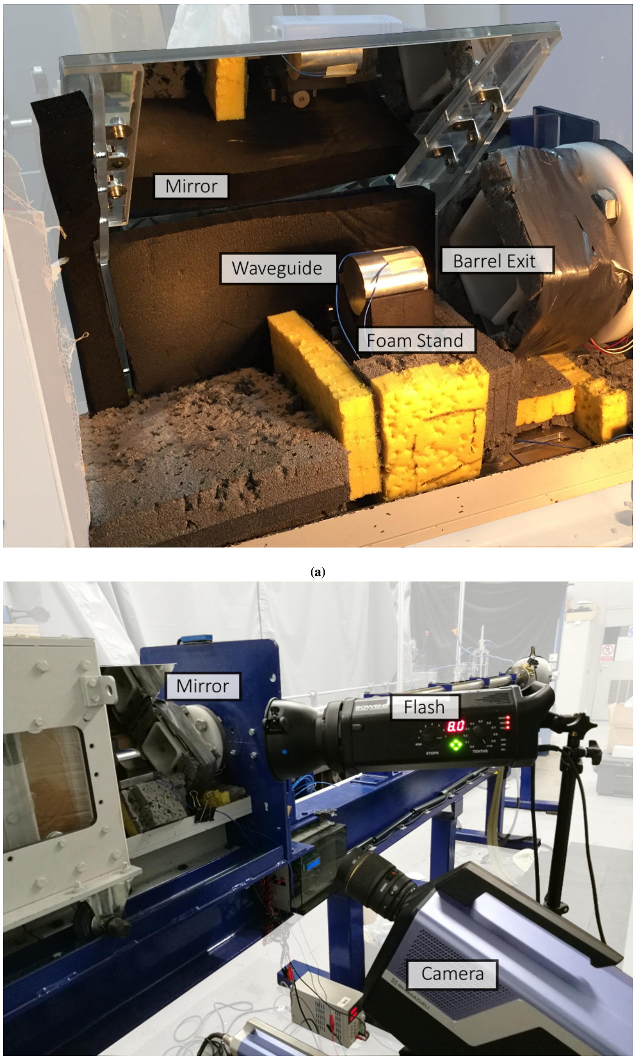

(a)

(b)

FIGURE 15 Mirror system installed in the capture chamber to enable visualisation of the impact in the ’top-down’ perspective. a) mirror installed in the chamber, b) camera setup to visualise mirror through side windows of the test chamber

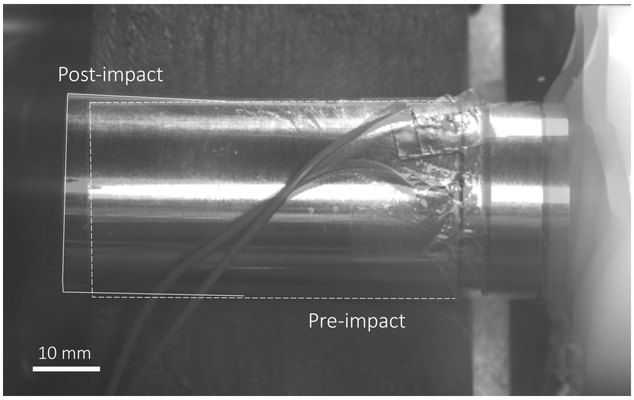

FIGURE 16 Image of waveguide position after misaligned impact overlaid on a static image 'pre-impact' showing the effect on the out-of-plane waveguide dynamics. Note that the pre-impact and post-impact positions are outlined in dashed and solid lines, respectively and that impact occurs from right to left.

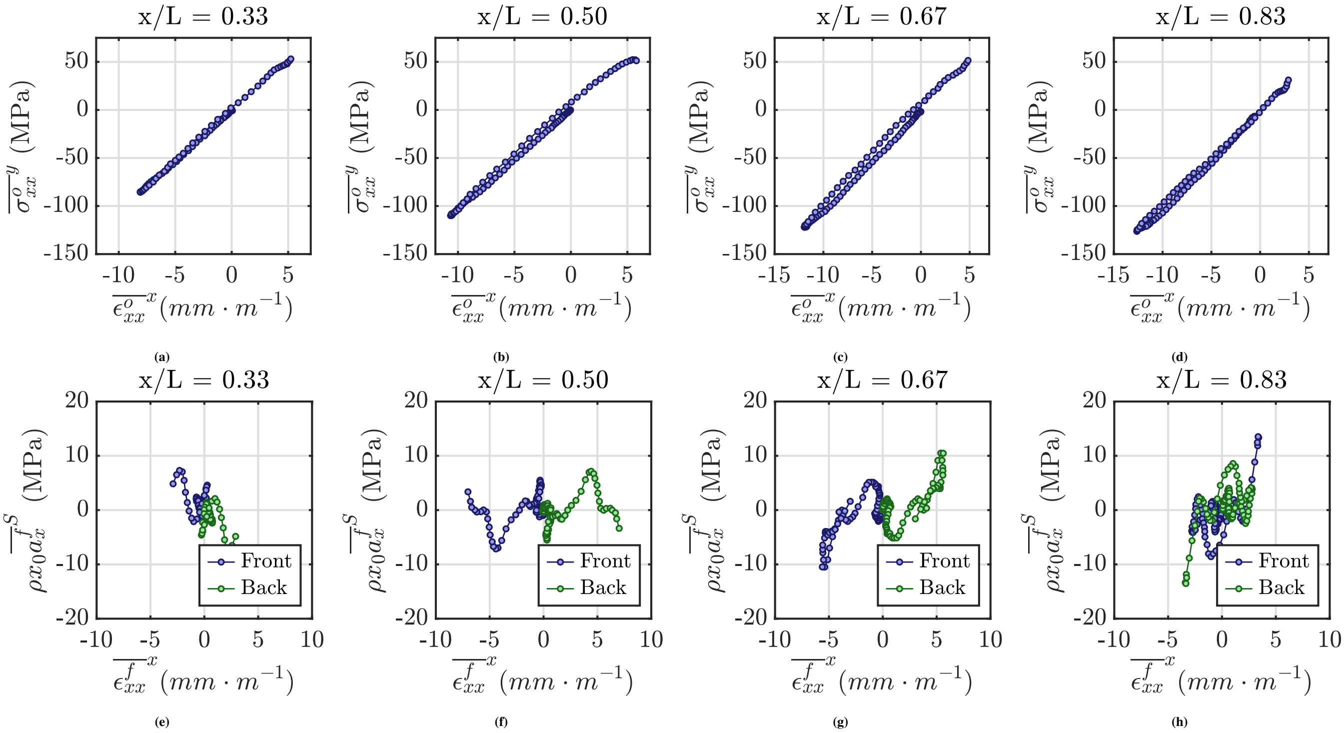

FIGURE 17 Stress-strain curves for specimen #1 reconstructed from decoupled membrane ((a)-(d)) and flexural ((e)-(h)) components of in-plane strain and acceleration

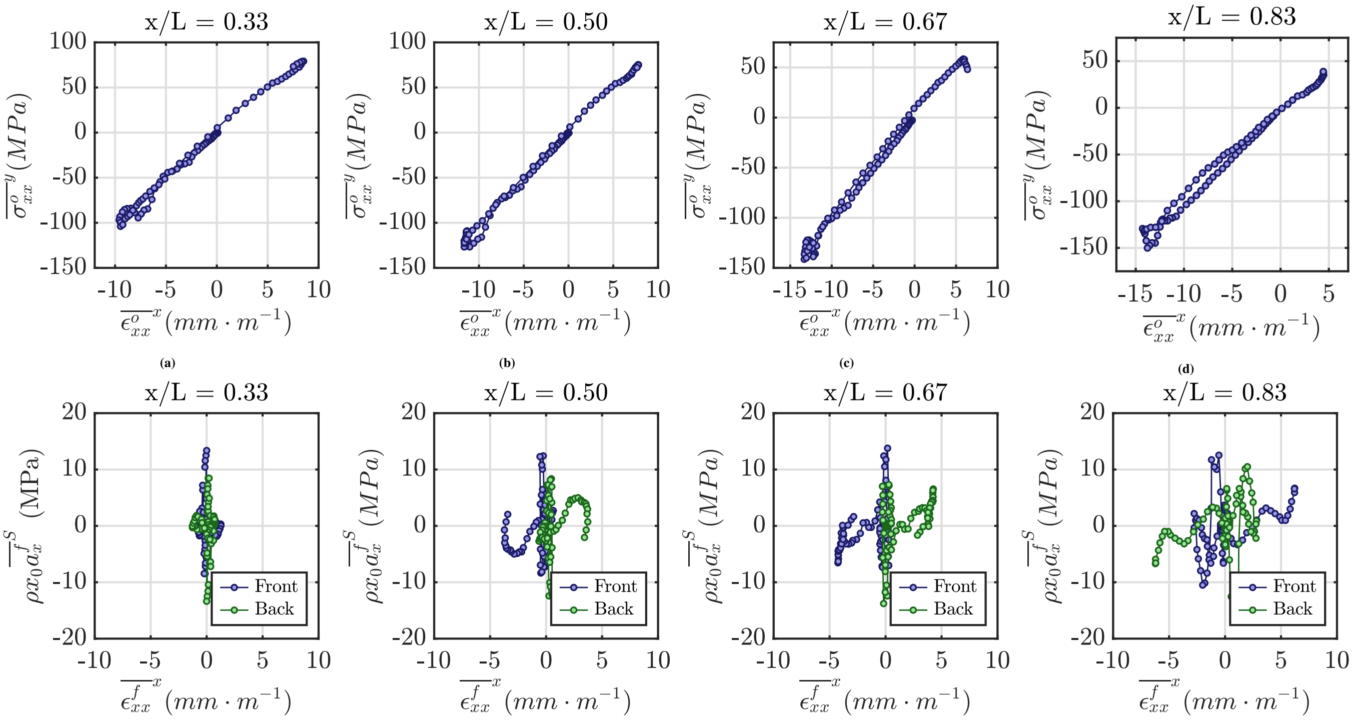

(a) (b) (c) (d)

(e) (f) (g) (h)

FIGURE 18 Stress-strain curves for specimen #3 reconstructed from decoupled membrane ((a)-(d)) and flexural ((e)-(h)) components of in-plane strain and acceleration

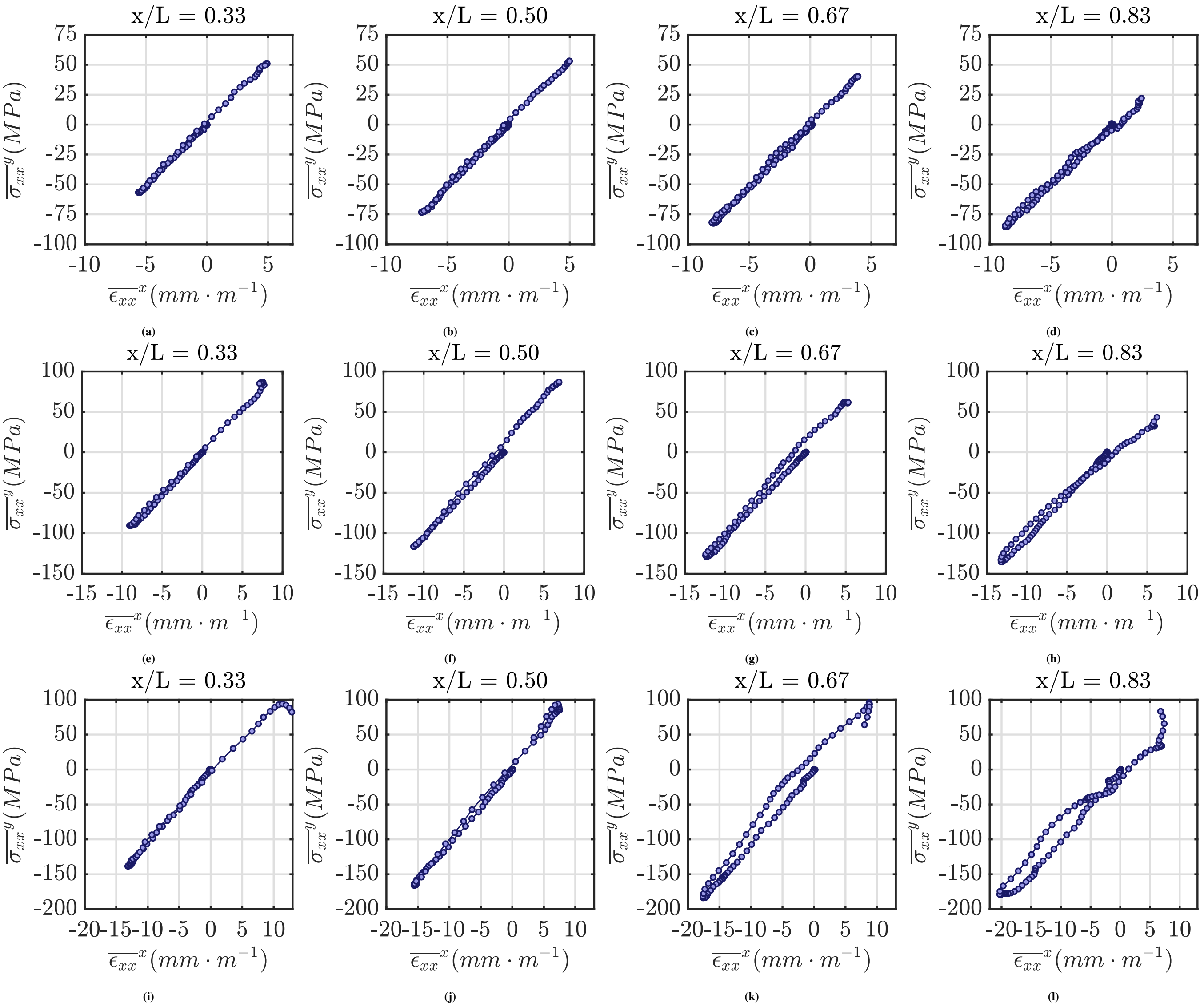

(a) (b) (c) (d)

(e) (f) (g) (h)

(i) (j) (k) (l)

FIGURE 19 Stress-strain curves for specimens tested with improved alignment as reconstructed with the stress-gauge equation: (a)-(d) R7 (25 m·s^{-1}), (e)-(h) R6 (35 m·s^{-1}), and (i)-(l) R4 (50 m·s^{-1})

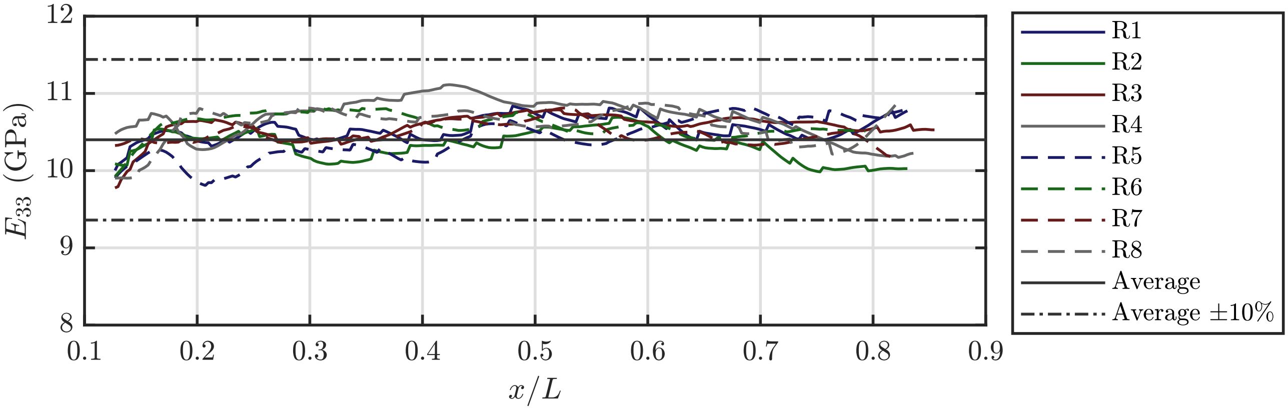

FIGURE 20 Spatial identifications for all specimens tested with the new alignment procedure. Note that E_{33} is determined with a linear fitting to the initial compressive loading behaviour up to 8 mm·m^{-1}

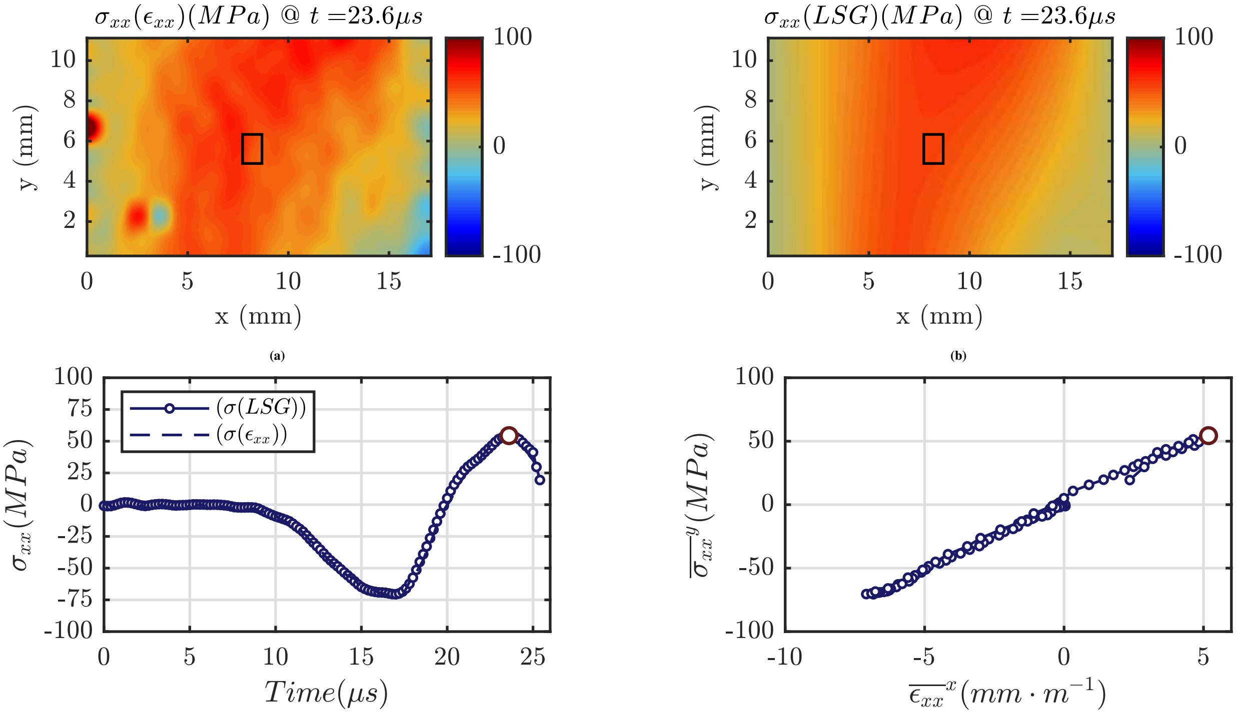

(a)

(b)

(c)

(d)

FIGURE 21 Failure stress identification diagnostics for sample R7 at $t = 23.6$ μs corresponding to the frame of maximum tensile stress in the centre of the sample: (a) stress field (MPa) constructed from ϵ_{xx}, using identified E_{33} ($\sigma_{xx}(\epsilon_{xx})$), (b) stress field (MPa) reconstructed using the linear stress-gauge equation ($\sigma_{xx}(LSG)$), (c) comparison of stress over time within the virtual gauge, (d) stress-strain curves reconstructed using average stress (linear stress-gauge) and strain within the virtual gauge. The virtual gauge is shown as the black rectangle in (a)-(b)

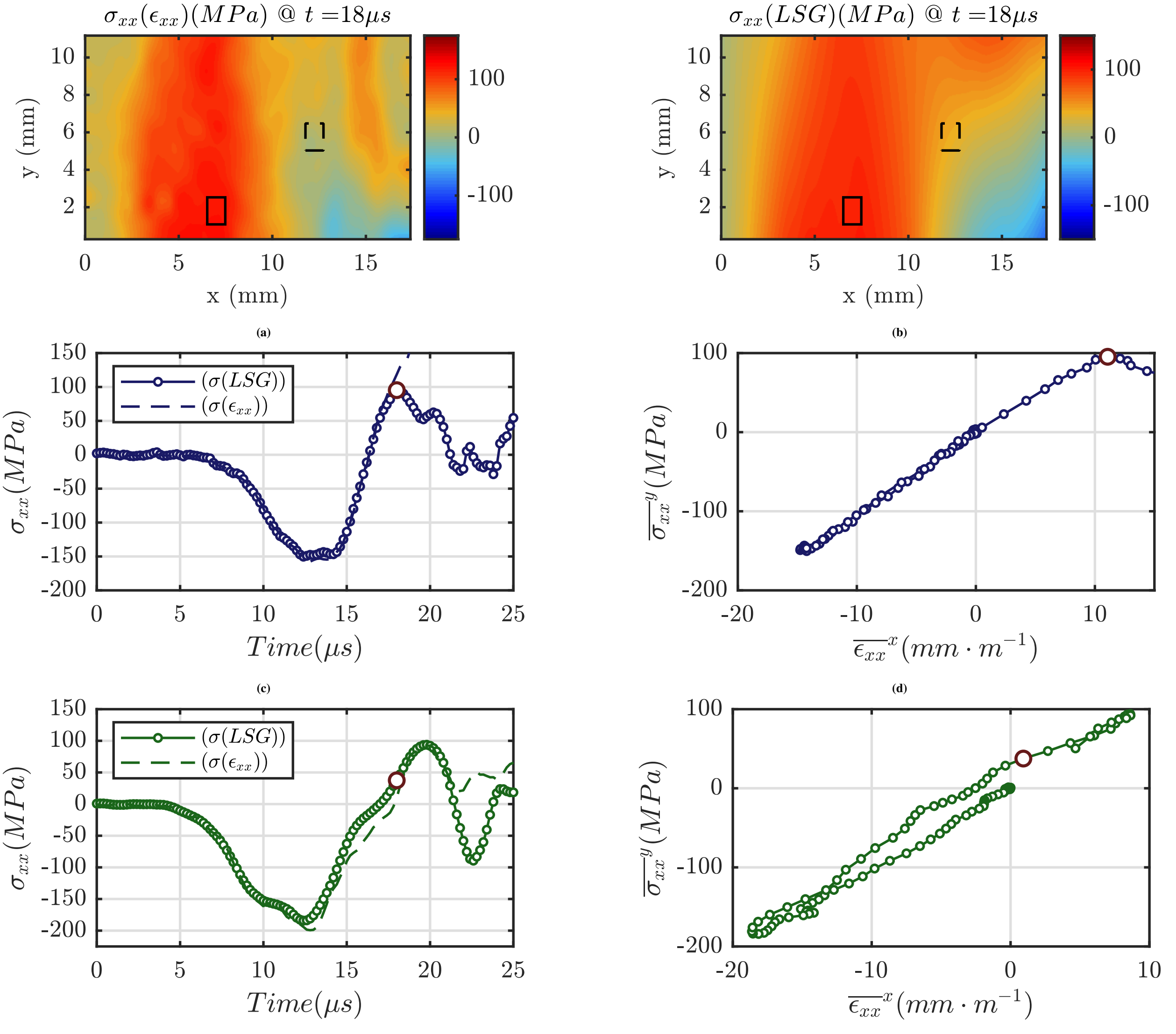

(a) (b) (c) (d) (e) (f)

FIGURE 22 Failure stress identification diagnostics for sample R4 at $t = 18$ μs corresponding to the frame of maximum tensile stress at the location of fracture: (a) stress field (MPa) constructed from ϵ_{xx}, using identified E_{33} ($\sigma_{xx}(\epsilon_{xx})$), (b) stress field (MPa) reconstructed using the linear stress-gauge equation ($\sigma_{xx}(LSG)$), (c) comparison of stress over time within the virtual gauge at the fracture location (solid rectangle in (a) and (b)), (d) stress-strain curves reconstructed using average stress (linear stress-gauge) and strain within the virtual gauge at the fracture location (solid rectangle in (a) and (b)), (e) comparison of stress over time within the virtual gauge at $x/L = 0.67$ (dashed rectangle in (a) and (b)), (f) stress-strain curves reconstructed using average stress (linear stress-gauge) and strain within the virtual gauge at $x/L = 0.67$ (dashed rectangle in (a) and (b)). The black rectangles in solid and dashed lines in (a)-(b) respectively represent the virtual gauge at the location of fracture, and in the region where the unloading and loading responses differed and non-linearity was measured at peak compression load

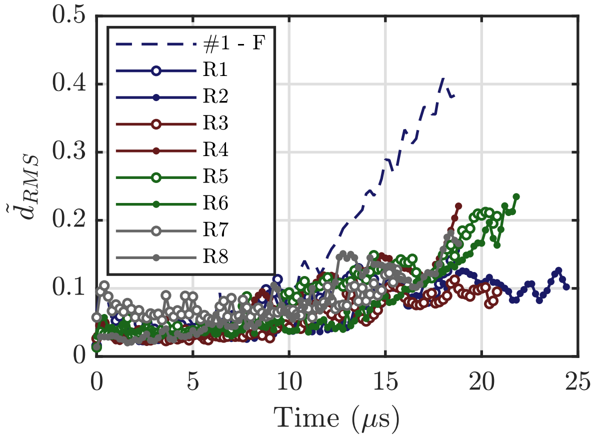

FIGURE 23 Temporal evolution of the normalised RMS difference between acceleration and strain-based stress reconstructions for specimens tested under improved alignment conditions compared to specimen #1 from the misaligned tests where bending effects were more significant (dashed line)

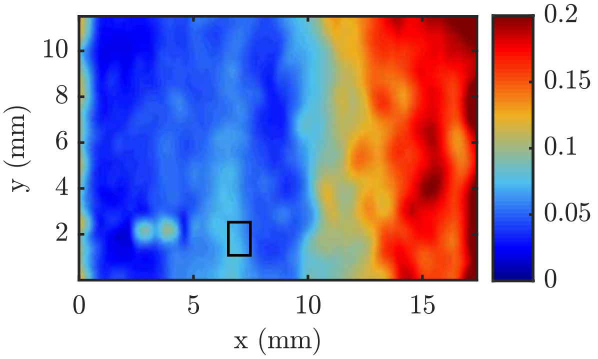

FIGURE 24 Full-field map of normalised RMS difference over time between acceleration and strain-based stress reconstructions for specimen R4. Note that the virtual gauge centred on the fracture location is shown as a black rectangle

TABLE 1 High-strain-rate interlaminar elastic modulus and tensile failure stress for AS4-145/MTM45-1 (1-3 plane) from front and back face measurements individually, and using back-to-back averaging

Specimen	E_{33} [GPa][a] Front (v_{RMS}(%))	E_{33} [GPa][a] Back (v_{RMS}(%))	E_{33} [GPa][a] Average† (v_{RMS}(%))	$\overline{\dot{\epsilon_{xx}}}$ [s^{-1}] (x10^3)[b] Front	$\overline{\dot{\epsilon_{xx}}}$ [s^{-1}] (x10^3)[b] Back	$\overline{\dot{\epsilon_{xx}}}$ [s^{-1}] (x10^3)[b] Average†	$\overline{\sigma_{xx}}^{VG}$ [MPa][c] Front	$\overline{\sigma_{xx}}^{VG}$ [MPa][c] Back	$\overline{\sigma_{xx}}^{VG}$ [MPa][c] Average†	$\overline{\dot{\epsilon_{xx}}}$ [s^{-1}] (x10^3)[d] Front	$\overline{\dot{\epsilon_{xx}}}$ [s^{-1}] (x10^3)[d] Back	$\overline{\dot{\epsilon_{xx}}}$ [s^{-1}] (x10^3)[d] Average†
1	9.9 (3.1)	11.5 (3.3)	10.6 (0.9)	-2.3	-2.0	-2.0	82.3*	67.6	65.0	2.4	5.3	3.6
2	10.2 (5.4)	10.8 (3.0)	10.5 (1.8)	-1.8	-1.5	-1.5	57.7*	49.5	44.5	1.4	3.8	2.6
3	10.5 (3.6)	10.6 (3.6)	10.5 (1.5)	-2.5	-2.3	-2.3	90.7*	84.1	81.4	3.6	6.8	5.2
4	10.9 (7.5)	10.3 (3.6)	10.6 (2.3)	-3.8	-4.7	-3.9	86.3	107.3*	95.6	8.9	8.1	8.5
5	9.9 (4.0)	11.5 (4.4)	10.5 (1.1)	-1.7	-1.6	-1.6	53.7*	63.3	53.6	2.3	4.2	3.3
6	11.0 (4.1)	10.9 (4.0)	11.0 (0.7)	-2.9	-2.6	-2.7	73.6*	65.4	66.5	5.1	6.6	5.8
7	11.0 (2.7)	10.9 (3.3)	11.0 (0.8)	-4.1	-3.7	-3.7	95.3*,**	71.8	72.3[x]	6.9	8.7	7.7[x]
Mean	10.5	10.9	10.7	-2.7	-2.6	-2.5	77.1	72.7	71.2	4.4	6.2	5.2
SD	0.50	0.38	0.21	1.0	1.1	1.0	16.1	18.4	19.2	2.8	2.2	1.9
COV (%)	4.7	3.5	2.0	63.3	44.8	43.3	20.9	25.3	27.0	25.6	29.9	43.8
Diff. to Q-S (%)	+33	+37	+35	–	–	–	+53	+44	+41	–	–	–

a: Stiffness identified from stress-strain curves
b: Strain rates reported as maximum width-averaged strain rate in compressive loading
c: Failure stress identified using linear-stress gauge equation, as detailed in Sec. 2.2
d: Strain rates reported as maximum averaged strain rate in virtual gauge up to frame before fracture
†: Back-to-back average of fields measured on the front and back faces to reconstruct the membrane component of stress (Sec. 2.3)
*: Crack appears first on other side of sample
**: Crack appears at different location to where crack appears first on other side of the sample
x: At crack location on back face

TABLE 2 High-strain-rate interlaminar elastic modulus and tensile failure stress for AS4-145/MTM45-1 (1-3 plane) with the revised alignment procedure

Specimen	V_{Impact} [m·s^{-1}]	E_{33} [GPa] (e_{RMS}(%))	$\overline{\dot{\epsilon_{xx}}}$ [s^{-1}]	$\overline{\sigma_{xx}}^{VG}$ [MPa]	$\overline{\dot{\epsilon_{xx}}}^{VG}$ [s^{-1}]
R1	54	10.5 (1.6)	-6,000	108.1	10,800
R2	51	10.3 (1.9)	-6,500	111.8	9,800
R3	51	10.5 (1.9)	-5,400	103.4	9,700
R4	50	10.9 (3.0)	-5,400	95.3	9,200
R5	37	10.3 (3.0)	-4,000	91.5	7,300
R6	35	10.7 (2.2)	-3,900	100.5	5,700
R7	25	10.5 (1.4)	-1,700	– *	3,300
R8	50	10.7 (2.5)	-5,800	99.3	9,200
Mean		10.4		103.6	
SD		0.23		7.0	
COV (%)		2.0		6.8	

*: No fracture